

REPORT DOCUMENTATION PAGE			FORM APPROVED OMB No. 0704-0188	
Public reporting burden for this collection of information is estimated to average 1 hour per response, including the time for reviewing instructions, searching existing data sources, gathering and maintaining the data needed, and completing and reviewing the collection of information. Send comments regarding this burden estimate or any other aspect of this collection of information, including suggestions for reducing the burden, to Washington Headquarters Services, Directorate for Information Operations and Reports, 1215 Jefferson Davis Highway, Suite 1204, Arlington, VA 22202-4302, and to the Office of Management and Budget, Paperwork Reduction Project (0704-0188), Washington, DC 20503.				
1. AGENCY USE ONLY (Leave blank)	2. REPORT DATE 12/23/94	3. REPORT TYPE AND DATES COVERED Final Report 14 Mar 90-30 Jun 94		
4. TITLE AND SUBTITLE Compressibility Effects on and Control of Dynamic Stall of Oscillating Airfoil			5. FUNDING NUMBERS ARO MIPR 103-94	
6. AUTHOR(S) M. S. Chandrasekhara				
7. PERFORMING ORGANIZATION NAME(S) AND ADDRESS(ES) Navy-NASA Joint Institute of Aeronautics. Code AA/CH Dept. of Aeronautics and Astronautics Naval Postgraduate School, Monterey, CA 93943			8. PERFORMING ORGANIZATION REPORT NUMBER	
9. SPONSORING/MONITORING AGENCY NAME(S) AND ADDRESS(ES) U. S. Army Research Office P.O. Box 12211 Research Triangle Park, NC 27709-2211			10. SPONSORING/MONITORING AGENCY REPORT NUMBER ARO 27894.27-EG	
11. SUPPLEMENTARY NOTES The view, opinions and/or findings contained in this report are those of the author(s) and should not be construed as an official Department of the Army position, policy, or decision, unless so designated by other documentation.				
12a. DISTRIBUTION/AVAILABILITY STATEMENT Approved for public release; distribution unlimited.			12b. DISTRIBUTION CODE DTC SELECTED MAR 13 1994	
13. ABSTRACT (Maximum 200 words) A three year effort to study the "Compressibility Effects on the Control of Dynamic Stall of Oscillating Airfoils" was funded by ARO in 1990. A fourth year extension was granted for the project. As part of this research, a new real-time interferometry system known as Point Diffraction Interometry (PDI) was developed. Several new and exciting details of the dynamic stall flow over an oscillating airfoil such as formation of multiple shocks were captured. The study also addressed the role of transition in influencing the dynamic stall process. A concurrent computational study was carried out to investigate the role of transition. Additionally, LDV measurements of the dynamic stall flow were obtained which support the PDI observations. A high speed PDI "movie" imaging system was designed to capture events of dynamic stall during a <i>single pitch-up</i> motion of the airfoil. This report describes the significant results obtained from the four year study of dynamic stall over an oscillating airfoil.				
14. SUBJECT TERMS Dynamic Stall, Compressibility Effects, Interferometry, LDV, Transition Effects			15. NUMBER OF PAGES 50	
			16. PRICE CODE --	
17. SECURITY CLASSIFICATION OF REPORT UNCLASSIFIED	18. SECURITY CLASSIFICATION OF THIS PAGE UNCLASSIFIED	19. SECURITY CLASSIFICATION OF ABSTRACT UNCLASSIFIED	20. LIMITATION OF ABSTRACT UL	

19950308 053

COMPRESSIBILITY EFFECTS ON AND CONTROL OF DYNAMIC STALL  
OF OSCILLATING AIRFOILS

FINAL REPORT

M.S.CHANDRASEKHARA

DECEMBER 23, 1994

U. S. ARMY RESEARCH OFFICE

ARO CONTRACT NUMBER: 27894-EG

Accession For	
NTIS CRASH	<input checked="" type="checkbox"/>
DTIC TAB	<input type="checkbox"/>
Unannounced	<input type="checkbox"/>
Justification	
By	
Distribution/	
Availability Codes	
Dist	Avail and/or Special
A-1	

DEPARTMENT OF AERONAUTICS AND ASTRONAUTICS  
NAVAL POSTGRADUATE SCHOOL  
MONTEREY, CA 93943

APPROVED FOR PUBLIC RELEASE  
DISTRIBUTION UNLIMITED

THE VIEW, OPINIONS, AND/OR FINDINGS CONTAINED IN THIS REPORT ARE  
THOSE OF THE AUTHORS AND SHOULD NOT BE CONSTRUED AS AN OFFICIAL  
DEPARTMENT OF THE ARMY POSITION, POLICY, OR DECISION, UNLESS SO  
DESIGNATED BY OTHER DOCUMENTATION

## FINAL REPORT

### Compressibility Effects on and Control of Dynamic Stall of Oscillating Airfoils

#### 1. FOREWORD

A three year effort to study the "Compressibility Effects on and Control of Dynamic Stall of Oscillating Airfoils" was funded by ARO in 1990. A fourth year extension was granted for the project. As part of this research, a new real-time interferometry system known as Point Diffraction Interferometry(PDI) was developed. Several new and exciting details of the dynamic stall flow over an oscillating airfoil such as formation of multiple shocks were captured. The study also addressed the role of transition in influencing the dynamic stall process. A concurrent computational study was carried out to investigate the role of transition. Additionally, LDV measurements of the dynamic stall flow were obtained which support the PDI observations. A high speed PDI "movie" imaging system was designed to capture events of dynamic stall during a *single pitch-up* motion of the airfoil. This report describes the significant results obtained from the four year study of dynamic stall over an oscillating airfoil.

Funding support received through MIPRs ARO-132-90, ARO-114-91, ARO-130-92, ARO-125-93, ARO-103-94 is gratefully acknowledged. This largely experimental study was conducted in the Fluid Mechanics Laboratory(FML) of NASA Ames Research Center. The support of FML Branch Chief, Dr. S.S.Davis and the cooperative participation of Dr. L.W.Carr, Group Leader, Unsteady Viscous Flows, U.S. Army AFDD & ATCOM are greatly appreciated. The project shared common instrumentation and facilities with projects carried out for AFOSR and NAVAIR Systems Command. The complementary support obtained for the development of these from the various agencies and the Naval Postgraduate School is also acknowledged.

## 2. TABLE OF CONTENTS

No.	Description	Page No.
1.	FOREWORD	1
2.	TABLE OF CONTENTS	2
3.	LIST OF FIGURES	4
4.A.	STATEMENT OF PROBLEM STUDIED	6
4.A.1	Nomenclature	6
4.A.2.	Description of the Experiment	7
4.A.2.1.	The Compressible Dynamic Stall Facility	8
4.A.2.2.	Instrumentation and Techniques	8
4.A.2.2.A.	Interferometry studies	8
4.A.2.2.B.	Interferogram Image Processing	9
4.A.2.2.C.	Determination of Pressure Coefficients by Fringe Counting	10
4.A.2.2.D.	LDV studies	11
4.A.2.2.E.	High Speed Imaging of Interferograms	11
4.A.2.3.	Tripping the Airfoil	12
4.A.2.4.	Experimental Conditions	14
4.A.2.5	Experimental Uncertainties	15
4.B.	SUMMARY OF MOST IMPORTANT RESULTS	15
4.B.1.	Flow Description from PDI Studies: Untripped Airfoil; $\alpha = 10^0 - 10^0 \sin \omega t$	15
4.B.1.A.	Dynamic Stall Flow Development	15
4.B.1.B.	Effect of Mach Number	16
4.B.1.C.	Delay of Stall Due to Unsteadiness	17
4.B.1.D.	Formation of Multiple Shocks	18
4.B.1.E.	Flow Reattachment	19
4.B.2.	Flow Description from LDV Studies: Untripped	

	Airfoil; $\alpha = 10^0 - 10^0 \sin \omega t$	21
4.B.2.A.	Phase Distribution of Ensemble Averaged Velocity Components	21
4.B.2.B.	Comparison of PDI and LDV Studies	22
4.B.3.	Flow Description from PDI and LDV Studies: Untripped Airfoil; $\alpha = 10^0 - 2^0 \sin \omega t$	23
4.B.3.A.	PDI Studies	23
4.B.3.B.	LDV Studies	24
4.B.4.	Tripped Airfoil Studies: Role of Transition in Large Amplitude Dynamic Stall	25
4.B.4.A.	Qualitative Analysis	25
4.B.4.B.	Quantitative Analysis	26
4.B.5.	Role of Adverse Pressure Gradient	27
4.B.6.	Conclusions	28
4.C.	LIST OF PUBLICATIONS AND TECHNICAL REPORTS	31
4.D.	LIST OF ALL PARTICIPATING PERSONNEL	34
5.	REPORT OF INVENTIONS	34
6.	BIBLIOGRAPHY	35
7.	ILLUSTRATIONS	38

### 3. LIST OF FIGURES

- Fig. 1. Side View of the Compressible Dynamic Stall Facility
- Fig. 2. Schematic of the Point Diffraction System
- Fig. 3. Schematic of Camera/Laser Synchronization for the High-Speed Phase-Locked Interferometry Imaging System
- Fig. 4. Schematic of the Unsteady Flow LDV Data Acquisition Method
- Fig. 5. Interferogram Sequence of Dynamic Stall Development Over an Oscillating Airfoil:  $M = 0.35$ ,  $k = 0.05$
- Fig. 6. Effect of Mach Number on Dynamic Stall: (a-d) PDI Images; (e-h) Global Pressure Fields
- Fig. 7. Effect of Unsteadiness on Airfoil Peak Suction Development:  $M = 0.3$
- Fig. 8. Comparison of Steady and Unsteady Airfoil Pressure Distributions:  $M = 0.3$
- Fig. 9. Effect of Unsteadiness on Airfoil Leading Edge Pressure Distribution:  $M = 0.3$ .
- Fig. 10. PDI Image of Multiple Shocks Over Untripped Oscillating Airfoil:  $M = 0.45$ ,  $k = 0.05$ ,  $\alpha = 10^\circ$
- Fig. 11. Global Pressure Field Over Untripped Airfoil from Image in Fig. 10
- Fig. 12. Interferograms of Reattachment Process:  $M = 0.3$ ,  $k = 0.05$ ; (a)  $\alpha = 12.27^\circ$ , (b)  $\alpha = 10.69^\circ$ , (c)  $\alpha = 9.84^\circ$ , (d)  $\alpha = 8.01^\circ$ .
- Fig. 13. Pressure Distributions During the Reattachment Process:  $M = 0.3$ ,  $k = 0.05$
- Fig. 14. Variation of Airfoil Suction Peak During the Reattachment Process:  $M = 0.3$ ,  $k = 0.05$
- Fig. 15. Schematic of the Reattachment Process
- Fig. 16. Phase Distribution of Velocity:  $\alpha = 10^\circ - 10^\circ \sin \omega t$ ,  $M = 0.3$ ,  $k = 0.05$ ; (a) Streamwise Component- U, (b) Vertical Component-V

- Fig. 17. Comparison of LDV and PDI Data:  $M = 0.3$ ,  $k = 0.05$ ,  $\alpha = 10^\circ$
- Fig. 18. PDI Sequence of Flow Over Oscillating Airfoil:  $M = 0.3$ ,  $k = 0.05$ ,  $\alpha = 10^\circ - 2^\circ \sin \omega t$
- Fig. 19. Contours of Z-component of Vorticity During Airfoil Downstroke:  $M = 0.3$ ,  $k = 0.05$ ,  $\alpha = 10^\circ - 2^\circ \sin \omega t$ ; (a)  $\alpha = 11.53^\circ$ , (b)  $\alpha = 11.0^\circ$
- Fig. 20. PDI Images of Untripped and Tripped Flow Fields:  $M = 0.3$ ,  $k = 0.05$   $\alpha = 10^\circ - 10^\circ \sin \omega t$ . Top Row: Untripped Airfoil, Bottom Row: Tripped Airfoil, (a,b)  $\alpha = 10.0^\circ$ , (c,d)  $\alpha = 13.99^\circ$
- Fig. 21. Effect of Tripping on Airfoil Peak Suction Development:  $\alpha = 10^\circ - 10^\circ \sin \omega t$ ,  $k = 0.05$ ; (a)  $M = 0.3$ , (b)  $M = 0.45$
- Fig. 22. Global Pressure Field of Shock Flow Over Tripped Airfoil:  $M = 0.45$ ,  $k = 0.05$ ,  $\alpha = 10.0^\circ$
- Fig. 23. Comparison of Surface Pressure Distributions Over Oscillating Airfoil in Untripped, Tripped and High Reynolds Number Flows:  $M = 0.3$ ,  $k = 0.05$ ,  $\alpha = 10^\circ - 10^\circ \sin \omega t = 10.0^\circ$
- Fig. 24. Mach Number Effect on Leading Edge Adverse Pressure Gradient Development on Transiently Pitching Tripped Airfoil:  $\alpha^+ = 0.03$
- Fig. 25. Leading Edge Adverse Pressure Gradient Development Over Untripped and Tripped Oscillating Airfoil:  $M = 0.3$ ,  $k = 0.05$

## 4.A. STATEMENT OF PROBLEM STUDIED

Dynamic stall is a particularly severe problem that occurs over the retreating blade of a helicopter and has in essence limited the flight envelope of the vehicle. Compressibility effects begin to appear at a forward flight Mach number of as low as 0.2 due to the large local flow acceleration around the blade leading edge. A significant effect of the onset of compressibility is premature flow separation that could be brought about by formation of local shocks. Even in cases where shocks do not form, the locally transonic flow seems to stall at lower angles of attack than if the flow were subsonic. Dynamic stall is a complex case of unsteady flow separation whose underlying physical processes are still not understood sufficiently. This is especially true when compressibility effects dominate the flow. The process starts out with the coalescing of the boundary layer vorticity into a dynamic stall vortex during the pitch-up portion of the blade oscillation cycle. As can be expected, the identification and quantification of a trigger that causes dynamic stall to occur is very difficult. That light dynamic stall could occur even at angles of attack *below* the static stall angle suggests that the process is vorticity dominated with gross mismatch between the time scales of vorticity diffusion through the boundary layer and that of the imposed unsteadiness of the airfoil through the oscillation cycle. However, since the parameter space of a helicopter blade operating conditions is very wide, the task of isolating the relevant flow physics is a very challenging task. The aim of the research was to systematically investigate the flow experimentally and identify some of the factors that directly affect the dynamic stall process. This was accomplished by studying dynamic stall of an NACA 0012 airfoil with 7.62cm chord whose angle of attack was varied as ( $\alpha = 10^\circ + 10^\circ \sin\omega t$  or  $\alpha = 10^\circ + 2^\circ \sin\omega t$  depending upon the experiments, see Sec. 4.A.2.4.) in flows with free stream Mach numbers ranging from 0.2 to 0.45 and at reduced frequencies from 0 to 0.1.

### 4.A.1. Nomenclature

$C_p$	pressure coefficient
$C_{p_{min}}$	peak pressure coefficient

c	airfoil chord
f	frequency of oscillation, Hz
k	reduced frequency = $\frac{\pi f c}{U_\infty}$
L	test section span
M	free stream Mach number
n	refractive index
$n_r$	refractive index at reference conditions
$n_0$	refractive index at atmospheric conditions
U,V	velocity components in the x and y directions
$U_\infty$	free stream velocity
x,y	chordwise and vertical distance
z	spanwise distance
$\alpha$	angle of attack
$\alpha_0$	mean angle of attack
$\alpha_m$	amplitude of oscillation
$\overline{\Delta PL}$	average path length difference
$\epsilon$	fringe number
$\lambda_0$	wavelength of the laser
$\rho$	density
$\rho_0$	density at atmospheric conditions
$\rho_r$	density at reference conditions
$\phi$	phase angle of oscillation
$\omega$	circular frequency, radians/sec

#### 4.A.2. Description of the Experiment

The experimental studies were carried out in the the compressible dynamic stall facility(CDSF) located in the Fluid Mechanics Laboratory(FML) of NASA Ames Research Center. NASA and FML provided much of the instrumentation needed for the research. Nonintrusive optical flow measurement techniques were used in the study. A brief descrip-

tion of the facility and measurement techniques is given below.

#### 4.A.2.1. The Compressible Dynamic Stall Facility

The CDSF is an indraft wind tunnel with a 25cm X 35cm test section and is equipped with a drive for producing sinusoidal variation of the airfoil angle of attack. The flow in the tunnel is controlled by a choked, variable area downstream-throat, to obtain a Mach number range of  $0 \leq M \leq 0.5$ . The flow is produced by a 6MW,  $108m^3/s$ , continuously running evacuation compressor. The airfoil mean angle of attack can be set to  $0 \leq \alpha \leq 15^\circ$ , the amplitude of oscillation to  $2^\circ \leq \alpha_m \leq 10^\circ$ , and the oscillation frequency to  $0 \leq f \leq 100Hz$ . The uniqueness of the CDSF is that a 7.62cm chord NACA 0012 airfoil is supported between two 15cm diameter optical glass windows by pins smaller than the local airfoil thickness. This permits optical access to the airfoil surface everywhere, for flow exploration using nonintrusive diagnostic techniques. The instrumentation includes a stroboscopic schlieren flow visualization system and a multi-component LDV system with associated hardware for unsteady flow measurements and a real time interferometry system. Fig. 1 shows the facility. Additional details of the facility are given in Ref. 1.

#### 4.A.2.2. Instrumentation and Techniques

The techniques of stroboscopic schlieren, stroboscopic point diffraction interferometry and two component, phase averaged LDV were used in the study. The data being reported were obtained using the latter two techniques which are briefly described below.

##### 4.A.2.2.A. Interferometry studies

Quantitative flow field density information was obtained using a newly developed interferometry technique known as *Point Diffraction Interferometry(PDI)*. The optical arrangement was similar to that of a standard Z-type schlieren system, but the light source was a laser beam expanded (to 15cm) to fill the field of view of interest in the test section. The optics were aligned to minimize astigmatism. The knife edge was replaced by a pre-developed (but not fixed), partially transmitting holographic plate (AGFA 8E75HD). This

was necessary to ensure that the emulsion remained soft in order to burn an appropriate sized pin-hole in it. Imaging optics were set up further downstream along the beam path for recording the flow as shown in Fig. 2. In operation, a pin hole was created *in situ* in the photographic plate with no flow in the test section. This acted as a point diffractor for the reference beam. Light refracted by the flow density changes (signal beam) focused to a slightly different spot (but partly over the point diffractor) and passed through the partially transmitting photographic plate, interfering with light passing through the pin-hole (which thus becomes the reference beam) to produce interference fringes in real time, which were then recorded on Polaroid film. Ref. 2 fully describes the technique and its implementation in the CDSF.

The Assistant Under Secretary of Defense, Dept. of Army, has recognized the development of the PDI technique by awarding the Army R & D Achievement award for 1991 to Dr. L.W.Carr, who is a co-operative participant in the project.

#### 4.A.2.2.B. Interferogram Image Processing

Several hundred interferograms were obtained during the experiment. In order to analyze the large number of interferogram images efficiently, special image processing software was developed. It runs on an IRIS Work Station. The present capabilities of the package include processing a digitized interferogram by allowing the user to start from marking the end points of a fringe, whose number is known and then marking the ends of the other fringes. In particular, the intersection of the various fringes with the airfoil surface are manually identified. The program then outputs a plot of the airfoil surface pressure distribution. Another similar package permits determination of the field pressure distribution. Attempts are underway to 'filter' out the noise in the images and also to automatically trace the fringes so that the surface and the global pressure distributions could be simultaneously determined. However, this is a challenging task since 'smartness' needs to be built-in to handle fringe discontinuities due to shocks, fringe distortions caused by steep density gradients (see Ref. 3), low contrast images, etc. The large density gradient around the leading edge causes the light rays to bend away from the region resulting in

near darkness there. However, upon graphically magnifying the images in the workstation, it was found that many could be traced closer to the airfoil than otherwise possible. A parallel (but larger) airfoil is then drawn to intersect the fringes. The intersection points with the different fringes are then transferred to the original airfoil by simple geometric scaling.

#### 4.A.2.2.C. Determination of Pressure Coefficients by Fringe Counting

For a standard interferometer, the path length difference  $\overline{\Delta PL}$  due to density (or phase) changes can be related to the fringe number  $\epsilon$  as,

$$\epsilon = \frac{\overline{\Delta PL}}{\lambda_0} = \frac{1}{\lambda_0} \int (n - n_r) dz$$

where  $n$  is the refractive index in the signal beam,  $n_r$  is that in the reference beam and  $\lambda_0$  is the wave length of the light used.

For a two-dimensional flow, the above equation can be simplified to,

$$\epsilon = (n - n_r) \frac{L}{\lambda_0}$$

where  $L$  is the test section span. If  $\epsilon$  is an integer, then the fringe is bright and if it is a half integer, the fringe is dark. Using the Gladstone - Dale equation and the perfect gas equation, the above equation can be reduced to

$$\rho - \rho_r = \left( \frac{\lambda_0}{n_0 - 1} \right) \left( \frac{\epsilon \rho_0}{L} \right) = A\epsilon$$

Since  $\lambda_0 = 532 \text{ nm}$ ,  $L = 25\text{cm}$ ,  $(n_0 - 1) = 2.733 \times 10^{-4}$  for air and  $\rho_0 = 1.21\text{kg/m}^3$ , the constant  $A$  can be determined. For the specific case of the present experiments,

$$\rho - \rho_r = A\epsilon = 0.009421\epsilon$$

or

$$\frac{\rho}{\rho_0} = \frac{\rho_r}{\rho_0} + \frac{A\epsilon}{\rho_0}$$

Since  $\frac{\rho_r}{\rho_0}$  is a function of the free stream Mach number only,  $\frac{\rho}{\rho_0}$  can be determined by knowing the fringe number. Note that in this method, a positive fringe number represents

deceleration and vice versa. Hence, fringes from the free stream to the stagnation point have positive values. The corresponding pressure along a fringe, including that at the boundary layer edge was derived using isentropic flow relations as:

$$C_p = \frac{\left[ \left( \frac{\rho}{\rho_r} \right)^\gamma - 1 \right]}{\left[ \frac{\gamma}{2} M^2 \right]}$$

The pressure at the edge of the boundary layer was then used as the surface pressure under the boundary layer assumptions.

#### 4.A.2.2.D. LDV studies

A two-color, two-component, frequency-shifted, Argon-Ion laser based, off-axis, forward-scatter, TSI system was used for velocity measurements. Traversing was accomplished by directing the 4 beams on to a 352mm focal length lens mounted on a computer controlled traverse. The signals were processed by TSI 1990 counters.  $1\mu m$  polystyrene latex particles suspended in alcohol injected from the tunnel inlet were used for seeding. Special phase locking circuitry enables handling of the random LDV data and the unsteady position data. The velocities were acquired in the coincidence mode with the window width arbitrarily set to  $50\mu sec$ . The coincidence pulse was used to trigger data acquisition and freeze the rapidly changing encoder values until data transfer to the computer was completed as shown in Fig. 3. The data acquisition and processing software incorporated the standard tests of data validation, ensemble averaging by binning the data appropriately, identifying holes in the data if the number of samples in any bin was less than a preselected value (50 in this case) and providing phase distributions of the velocity components. Any time the standard criteria were not satisfied, the data set was rejected and a new set acquired. A minimum of 10,000 samples were collected per channel at each measurement point. The complete details of the scheme can be found in Chandrasekhara and Ahmed<sup>4</sup>.

#### 4.A.2.2.E. High Speed Imaging of Interferograms

Since there is cycle to cycle variations in the details of the dynamic stall process, it was decided to document the occurrence of dynamic stall through a single oscillation cycle

of the airfoil. This necessitated the design of an integrated imaging system to synchronize the laser, the camera and the phase locking/trigger system. The design was carried out for a similar need for the AFOSR sponsored project and is described in Ref. 5. The laser used was externally triggered by TTL pulses generated by a Cordin high speed drum camera. The camera houses a rotating 8-faceted mirror which reflects the images on to a film rotating with the drum for recording. A custom built (in-house) electronic circuitry generated the required TTL pulses for triggering the laser. The system was tuned by using an infrared (IR) emitter and detector, which detected the mirror facets as they passed as shown in Fig. 4. The detector beam was not in the optical path of the camera and the film was not sensitive to the 940nm IR wavelength. During the tuning process, once a mirror facet was detected by the IR detector, two other photo detectors placed - one at frame position - produced delayed TTL pulses (the delays were adjusted suitably depending on the camera framing rate) which were subsequently used for synchronizing the camera shutter with the laser pulsing. In actual use, the photo detectors were moved out of the light path. Additional electronics to initiate the data acquisition from a desired angle of attack of the oscillating airfoil were also developed and integrated with the phase locking circuitry used for stroboscopic interferometry.

#### 4.A.2.3. Tripping the Airfoil

Results from the first phase of the study showed that dynamic stall originates out of the bursting of the laminar separation bubble that formed over the oscillating airfoil, leading to the conclusion that transition and low Reynolds number dynamic stall are intricately coupled. Thus, the study was refocused with the goal to identify the role transition plays in influencing the dynamic stall process. This, however, is not an easy task given that under compressible conditions, dynamic stall starts at the leading edge, where the boundary layer is in a transitional state, even in high (chord based) Reynolds number flows. Further, the transition point moves closer to the leading edge with increasing angle of attack and the transition length decreases with the concomitantly increasing adverse pressure gradient. Thus, it is likely that the boundary layer will, at best, be in its *early-turbulent* state

when the dynamic stall is initiated. Both experimental and computational modelling of this situation are extremely difficult. The challenge is to produce a distributed roughness system that satisfactorily trips the flow, yet is smaller than the local boundary layer thickness, which in the present experiments was estimated to be about  $60\mu m$  at the point of flow separation ( $x/c = 0.02$  to  $0.04$ ). Ref. 6 details the effort and in the following, only the key aspects are discussed.

A review of literature <sup>7,8</sup> was conducted to obtain the first estimate of the required trip size. The leading-edge-stalling NACA 0012 airfoil flow bears considerable qualitative similarity to the flow over a circular cylinder. Therefore, it was decided to use a roughness strip as the tripping device following the recommendations of Nakamura and Tomonari<sup>7</sup>. A formula given in Ref. 8 was used to arrive at the minimum size of the trip for the boundary layer. As reported in Wider et al<sup>9</sup>, this formula indicated a grit size diameter of  $56 - 89\mu m$  ( $0.0022 - 0.0035$ in.) for  $0.2 \leq M \leq 0.3$ . Boundary layer transition trips were formed by bonding three-dimensional roughness elements in a spanwise strip of height  $170\mu m$  along the surface of the airfoil. Wind tunnel tests were performed with this trip (trip 1) in place. The results indicated premature stall<sup>9</sup>, attributable to the large trip height resulting from the fabrication process used. Thus, it became necessary to conduct a systematic investigation and perform tests with different trip heights to identify a trip that yielded acceptable results. A total of five trip configurations having the following characteristics were tested:

Trip 1.  $74 - 89 \mu m$  diameter carborundum grains (number 220 polishing grit) were bonded to the airfoil surface using a water-soluble-adhesive (Polaroid print-coating material). The strip was located on the upper surface for  $0.005 \leq x/c \leq 0.03$ . The average height of the trip was  $170 \mu m$ .

Trip 2. A repeat of trip number 1 using a spray-on enamel lacquer adhesive. The average height of this trip was  $100 \mu m$ . The lacquer was used for all subsequent trips.

Trip 3. Made of the same materials as trip number 2, this strip covered the entire leading edge starting on the lower surface at  $x/c = 0.05$  (near the mean stagnation point) and extending to the upper surface at  $x/c = 0.03$ . The average height was approximately  $130 \mu m$ .

Trip 4. A smaller grit material, 22 - 36  $\mu m$  aluminum oxide particles, was used for trips 4 and 5. Trip number 4 was located on the upper surface,  $0.005 \leq x/c \leq 0.03$ , like trips 1 and 2. The trip was estimated to be no higher than 43  $\mu m$ .

Trip 5. The last trip extended from  $x/c = 0.05$  on the lower surface around the leading edge to  $x/c = 0.05$  on the upper surface. The trip height was approximately 40 - 50  $\mu m$ .

In each case the trip height was estimated from digitized airfoil images taken under no-flow conditions by magnifying and scaling the images on an IRIS workstation. The uncertainty in the estimated trip heights is  $\pm 10\mu m$ . The boundary layer height was estimated to be about 60 $\mu m$  at the point of flow separation ( $x/c = 0.02$  to 0.04).

#### 4.A.2.4. Experimental Conditions

Most of the experiments were conducted for a flow Mach number range from  $0.2 \leq M \leq 0.45$ . The corresponding Reynolds number ranged from 360,000 - 810,000. The oscillation frequency was varied from 0 - 60Hz, resulting in reduced frequencies from 0 - 0.10. The airfoil was oscillated about the 25% chord point, with its angle of attack varying as  $\alpha = 10^\circ - 10^\circ \sin \omega t$ . Thus, phase angle,  $\phi = 0^\circ$  corresponded to  $\alpha = 10^\circ$ ,  $90^\circ$  to  $\alpha = 0^\circ$  on the airfoil downstroke,  $180^\circ$  to  $\alpha = 10^\circ$  on the upstroke and  $270^\circ$  to the maximum angle of attack of  $20^\circ$ . The LDV probe volume was traversed in the range  $-0.25 \leq \frac{x}{c} \leq 0.75$ ,  $0.0 \leq \frac{y}{c} \leq 0.58$ . A large number of interferograms were obtained at close intervals depending on the event being imaged. The interval was less than 0.1 degrees (one encoder count) during initiation of the dynamic stall process. Both full flow field and leading edge region were separately studied.

Additional LDV studies were also carried out for just the leading edge region, for two amplitudes, viz. 2 degrees and 10 degrees, in the region  $-0.25 \leq \frac{x}{c} \leq 0.25$ ,  $0.083 \leq \frac{y}{c} \leq 0.167$ . Some PDI data was obtained for the case of  $\alpha = 10^\circ - 2^\circ \sin \omega t$  also.

The tripped airfoil studies were compared with the untripped airfoil flows in both steady and unsteady (10 deg. amplitude) flows, for  $k = 0.05$  and 0.1 at  $M = 0.3$  and for  $k = 0.05$  at  $M = 0.45$ .

#### 4.A.2.5 Experimental Uncertainties

The estimated uncertainties are as follows:

Mach number:	$\pm 0.005$
angle of attack:	0.05 degrees
reduced frequency:	0.005
$C_{p_{min}}$ :	$\pm 0.075$ at $M = 0.3$ $\pm 0.0375$ at $M = 0.45$
$\frac{dC_p}{d(x/c)}$	$\pm 15$

The uncertainty in  $C_p$  depends on the fringe number under consideration and is estimated to be 1 fringe for the flow in general with about 3 fringes possibly undetectable near the suction peak.

The uncertainty in the LDV data is estimated to be about 5% in attached flow. The corresponding uncertainty in calculated vorticity is about 25%.

### 4.B. SUMMARY OF MOST IMPORTANT RESULTS

#### 4.B.1. Flow Description from PDI Studies: Untripped Airfoil;

$$\alpha = 10^\circ - 10^\circ \sin \omega t$$

##### 4.B.1.A. Dynamic Stall Flow Development

The details of the development of dynamic stall have been discussed in Ref. 10 - 12. The following discussion has been summarized from Ref. 12. Figure 5 (Ref. 10) shows a sequence of interferograms obtained over the oscillating airfoil for  $M = 0.35$  and  $k = 0.05$ . The fringes seen in it are constant density contours of the flow. The stagnation point is on the airfoil lower surface, near the leading edge and the fringes are seen to converge here. At  $\alpha = 10.65^\circ$ , (Fig. 5a) a moderately thick boundary layer is seen near the trailing edge. The fringes indicate that there is a slight local trailing edge separation; however, it appears to have no measurable effect on the overall flow. The fringes at  $\alpha = 12.11^\circ$  (seen in Fig. 5b), after radiating from around the leading edge, turn towards the airfoil upper

surface downstream of the suction peak. But, when they encounter the local boundary layer, they turn sharply again towards the trailing edge. A closer examination reveals that there is a small region on the upper surface near the leading edge which is enclosed by the fringes that physically appears like a bubble. Pressure distributions (see Ref. 12) deduced from the interferograms confirm that a laminar separation bubble is present under these conditions. As the angle of attack is increased, the bubble breaks down and a vortical structure appears at  $\alpha = 12.83^\circ$ . The static stall angle for  $M = 0.35$  is  $11.6^\circ$  and thus, the first indication that the dynamic stall *delay* has ended and the dynamic stall process *itself* has begun is seen in Fig. 5d,  $1.2^\circ$  beyond static stall. The events that lead to the formation of dynamic stall vortex occur very rapidly from this angle of attack, in a very small angle of attack range, (less than one degree, shown in Fig. 5b - 5d). Thus, the complete details of the changes are not easy to capture; the rapidity of the process and possible cycle-to-cycle variations make it a very challenging measurement problem. The earlier schlieren data showed that the deep dynamic stall angle for this case was  $15.2^\circ$ ; thus, by  $\alpha = 16.02^\circ$ , deep dynamic stall has already occurred. However, the number of fringes on the lower surface near the trailing edge shows that sharp gradients are still present there. The subsequent trailing edge flow evolution (such as vortex shedding, the occasional propagation of the vortex upstream over the airfoil upper surface (Ref. 13), etc.) influences the other details aspects of the separated flow like reattachment, hysteresis loops, etc.

#### 4.B.1.B. Effect of Mach Number

Figure 6<sup>12</sup> presents interferograms for  $M = 0.3, 0.35, 0.4$  and  $0.45$ , obtained at  $k = 0.05$  and  $\alpha = 12.06^\circ$ . Fig. 6a at  $M = 0.3$ , shows a laminar separation bubble in its early stages of bursting at this angle of attack. But, this event is not yet felt in the outer flow and hence, is not detectable there. Fig. 6b, at  $M = 0.35$ , shows the formation of vertical fringes from  $x/c = 0.04$  to  $x/c = 0.15$ . It has been shown in Ref. 13 that this state represents the onset of dynamic stall and that the vortex is in its incipient stages of formation. The outer flow still is not affected by the major changes in the flow field close to the airfoil. At

$M = 0.4$ , (Fig. 6c) the dynamic stall vortex has fully developed and has convected over the airfoil surface; it should be pointed out that the imprint of the dynamic stall vortical region in compressible flow is not circular, but some what oval in shape. The outer edge of the vortex has reached about 30% chord; further downstream, the boundary layer has grown considerably in size. In contrast, Fig. 6d shows that at  $M = 0.45$ , the dynamic stall process has progressed to an extent where the vortex edge has already convected beyond  $x/c = 0.5$ . In fact, deep dynamic stall occurred for  $M = 0.45$  and  $k = 0.05$  at  $\alpha = 14.2^\circ$  but for  $M = 0.3$ , the corresponding angle was  $15.9$  deg. The global pressure data is shown in Fig. 6e - 6h. The peak suction drops from  $-5.67$  at  $M = 0.3$  to  $-3.01$  at  $M = 0.45$ . It is believed that the errors introduced by the use of isentropic flow assumptions in the presence of a dynamic stall vortex do not result in a different interpretation of the results at these Mach numbers. The dramatic influence of the vortical flow on the outer inviscid flow is clearly seen in Fig. 6g and Fig. 6h.

#### 4.B.1.C. Delay of Stall Due to Unsteadiness

Figure 7<sup>12</sup> shows the peak suction pressure coefficient,  $C_{p_{min}}$  plotted as a function of angle of attack for  $M = 0.3$ , for steady flow ( $k = 0$ ) and the unsteady flow cases of  $k = 0.05$  and  $0.1$ . The distribution for steady flow shows abrupt leading edge stall that is typical of NACA 0012 airfoil. The curves for the unsteady cases show a delay of stall from that of steady flow, which increases with  $k$ . This clearly points out that the airfoil develops less suction at comparable angles of attack and thus, the airfoil experiences a lesser adverse pressure gradient with increasing unsteadiness. The peak suction eventually reaches a value higher than that in steady flow, although the resultant adverse pressure gradient may not be much higher (see Fig. 9). It has been shown in Ref. 13 that for a transiently pitching airfoil, the suction pressure coefficient remains at the maximum value during the time when the dynamic stall vortex forms and organizes, and then drops as the vortex convects down the airfoil; the same result is seen for the oscillating airfoil also. The organization time seems to depend on the reduced frequency, since the amount of coherent vorticity introduced by the airfoil motion also depends on  $k$ . So, it can be expected that at

higher reduced frequencies, the plateau seen in the  $C_{p_{min}}$  distributions lengthens, leading to a longer stall delay; this effect can be seen in Fig. 7. The peak suction drops gradually once vortex convection begins.

Figure 8 compares the pressure distributions at  $M = 0.3$  between the steady flow at  $\alpha = 11.0$  deg and unsteady flow at  $k = 0.05$  at  $\alpha = 10.0^\circ$ . It is evident that the two compare very well, with only a slight deviation in the bubble region. The agreement indicates that the unsteady flow at a higher angle of attack is similar to steady flow at a lower angle of attack, prior to stall onset, pointing to a general delay of flow development in the unsteady flow. In this case for  $M = 0.3$ , and  $k = 0.05$ , this delay is one degree. The plateau seen in the distributions points to the existence of a laminar separation bubble, since the pressure along the bubble is constant. The pressure rises normally after the bubble closes. The bubble forms over the airfoil since the Reynolds number (360,000 - 840,000) of the flow is in the transitional regime. The other small differences are within the one fringe the uncertainty of the PDI technique.

Figure 9 presents the pressure distributions for  $0 \leq x/c \leq 0.04$  for  $k = 0, 0.05$  and  $0.1$  at  $\alpha = 10.0^\circ$  at  $M = 0.3$ . The plots show that the suction develops over an oscillating airfoil at a reduced rate as the frequency of oscillation is increased and in fact does not reach the steady state level at the angle compared. Past the suction peak, the pressure rises more slowly in the unsteady cases. This delay of the airfoil flow development, with corresponding delay in the development of the adverse pressure gradients can be seen to be one of the causes of dynamic stall delay that is observed. It should be noted that each symbol in Fig. 9 corresponds to a quantitative measure of the instantaneous pressure as obtained from the interferogram. This is the first set of data to show the lessening of the local adverse pressure gradient by unsteadiness in such detail and offers a reasonable explanation for the delay for stall.

#### 4.B.1.D. Formation of Multiple Shocks

For certain compressible flow conditions, (e.g.  $M = 0.45$ ,  $k = 0.05$ ,  $\alpha = 10^\circ$ ) a shock or a series of shocks formed near the airfoil leading edge as shown in Fig. 10. The  $\lambda$ -

shocks seen are characteristic of laminar flow behavior. Interestingly, the flow does not separate immediately once a shock forms. It seems to be able to withstand the local adverse pressure gradient caused by the shock for a small range of angle of attack before separating. A series of pictures for these experimental flow conditions showed that flow separation at the foot of the last shock eventually resulted in the dynamic stall vortex. At this time, the reason for the multiple shocks is still under investigation. It is believed that the first shock interacts with the laminar leading edge boundary layer introducing a waviness in the boundary layer thickness which seems to be sufficient for producing the expansion waves and compression waves necessary for the system to sustain itself during a small angle of attack sweep of the airfoil.

A map of the pressure coefficients obtained using isentropic flow assumptions in the vicinity of the multiple shocks for the case shown above is presented in Fig. 11. The leading edge region has been magnified so that the flow variations due to the shocks can be analyzed. This unique quantitative evaluation of the *outer flow* was made possible by the fringe tracing/analysis algorithm developed for the project. It is clear that the flow becomes supersonic near the surface and that a region of  $M > 1$  (the sonic line corresponds to  $C_p = -2.76$ ) which is significantly wider than previously thought exists in the flow. In this region, 5 shocks are present. The shocks terminate in the sonic line. The outer flow, however, is still subsonic. As the angle of attack is increased, the shock pattern changes since the interaction with the boundary layer changes. Eventually, a dynamic stall vortex appears at the foot of the last shock. The  $x/c$  location at which this happens is about 0.05 - 0.08, indicating that the dynamic stall vortex does not form at the leading edge. This figure attests to both the presence of the fine scale details in the flow as well as the ability of the measurement technique used in this research to capture them.

#### 4.B.1.E. Flow Reattachment

Whereas much attention has been devoted to the flow separation process leading to dynamic stall, the subsequent flow reattachment has generally been ignored by many researchers. The reattaching flow is very important to determine the hysteresis loop and aerodynamic damping. The present study was aimed at obtaining some information on

the reattachment phenomenon itself. Both PDI and LDV studies were carried out for the downstroke of the airfoil. Here, the PDI results will be discussed. Schlieren studies<sup>14</sup> of the flow showed that flow reattachment occurred over a range of angles of attack in case of an oscillating airfoil as opposed to a steady airfoil flow where it was either attached or separated at angles of attack very slightly below or above the static stall angle. PDI pictures presented in Fig. 12 for  $M = 0.3$  and  $k = 0.05$  show that the flow begins to reattach at  $\alpha = 12.27^\circ$  in Fig. 12a, but soon it separates downstream of the leading edge (Fig. 12b). Reattachment progresses further downstream gradually to  $x/c = 0.35$  in Fig. 12c as the airfoil angle of attack is reduced, with the process completing at  $\alpha = 8^\circ$ . To determine the development of the suction peak over the airfoil, a number of reattaching flow PDI images were obtained. Fig. 13 presents the airfoil surface pressure distributions corresponding to these images. Fig. 12c as well as the plateau in Fig. 13 confirm that a bubble forms during the process. Further, the airfoil peak suction increases as shown in Fig. 14 while the flow is reattaching, from near the static stall angle even when its angle of attack is decreasing until the process is completed at  $\alpha = 8.0^\circ$ . The peak suction decreases afterwards as the flow adjusts to the lower angles of attack. It is also interesting to note that the peak suction values are lower than the corresponding values on the upstroke when the flow is attached, as shown in Fig. 6 for  $k = 0.05$ , indicating large hysteresis. LDV studies<sup>14</sup> also indicated considerable hysteresis effects between the upstroke and the downstroke. Based on these data, a picture of the reattachment process was constructed which is shown in Fig. 15. The key features of flow reattachment are: it is a continuous process that starts at around the static stall angle. The flow then separates immediately. However, as the angle of attack is reduced, the process proceeds with the formation of a bubble as the suction peaks builds near the airfoil leading edge. The suction peak continues to increase until the process is completed and then decreases. The bubble eventually disappears at a lower angle of attack.

#### 4.B.2. Flow Description from LDV Studies: Untripped Airfoil;

$$\alpha = 10^\circ - 10^\circ \sin \omega t$$

##### 4.B.2.A. Phase Distribution of Ensemble Averaged Velocity Components

Fig. 16a<sup>15</sup> shows the variation of the streamwise velocity  $U$ , with phase angle at  $x/c = 0.067$  for  $\alpha = 10^\circ - 10^\circ \sin \omega t$ . Dramatic changes can be seen in the phase plots at  $y/c$  locations close to the airfoil surface. At  $y/c = 0.083$  during the downstroke, the velocity decreases to  $1.05U_\infty$  at  $\phi = 90^\circ$ ,  $\alpha = 0^\circ$ ; and begins to increase as expected during the upstroke of the airfoil. This is true for fluid layers at other heights as well. However, at  $\phi = 155^\circ$ ,  $\alpha = 5.5^\circ$ , the velocity drops rapidly to  $0.4U_\infty$  over  $155^\circ \leq \phi \leq 202^\circ$ , corresponding to  $5.5^\circ \leq \alpha \leq 13.7^\circ$ . Such a drop can be attributed to the presence of a separation bubble that penetrates the LDV probe volume as the airfoil pitches up. Some of these phase angle bins contained very few samples, but the data was accepted by verifying from the histograms that the velocities measured represented a normal physical process. Eventually at this location, the airfoil blocks off the beams and thus no data could be obtained until a phase angle of  $\approx 330^\circ$ . (This is the reason for the gaps in the distribution seen for some phase angles.) At the higher locations, the phase angle range over which this drop occurs decreases since the bubble is narrow at the top. Fig. 16a shows further that the bubble bursts between  $\phi = 200^\circ - 216^\circ$ . Measurements of the  $V$  component of velocity presented in Fig. 16b also show rapid increases in this phase angle range. In these figures, measurement points below  $y/c = 0.117$  are within the separation bubble. The phase variation seen at  $y/c = 0.133$  is typical of the variation seen in the outer points in the flow. The vertical velocity in the bubble is generally small,  $O(0.1U_\infty)$ . In steady flow leading edge type stall, bubble bursting is a rapid event. However, in the unsteady dynamic stall flow, it occurs over a small range of phase angles. Fig. 16b shows a gradually increasing  $V$  velocity until  $\phi = 216^\circ$ ,  $\alpha = 15.9^\circ$ , which is known to be the dynamic stall angle from earlier schlieren studies<sup>16</sup>. (The static stall angle for this Mach number is 12.4 degrees). At this angle of attack, the dynamic stall vortex is shed and the airfoil shear layer detaches from the surface everywhere, except at the leading edge. This causes a large  $V$  velocity and concurrently, the  $U$  velocity drops. These features are distinctly seen in Fig.

16a and 16b. No negative velocities were measured in the bubble because the reverse flow region was very thin (less than 1% chord high). It was very difficult to seed the region and also, optical access was not available due to the four-beam configuration used. Magnified interferograms also confirmed that the layer of reversed flow was indeed very thin.

The z-component of vorticity was calculated from the measured U and V components of velocity by first fitting a cubic spline curve to the data and interpolating the velocities in a grid at a resolution of 1.25mm - using a second order central differencing scheme. A calculation of the circulation over the airfoil around the measurement region (Ref. 4) showed an increase until the stall vortex convection was initiated and dropped slightly beyond this angle of attack.

The LDV data could only be obtained in the domain outside the airfoil boundary layer, especially near the leading edge. Here, the estimated boundary layer thickness was less than the LDV probe volume diameter. The very small boundary layer thickness and the large flow acceleration caused a lack of seed particles being present at points close to the surface near the airfoil leading edge, where dynamic stall originates. Thus, well resolved data could not be obtained in some critical regions of the flow.

#### 4.B.2.B. Comparison of PDI and LDV Studies

Since two different quantitative measurement techniques were used in the present study, it is instructive to make a direct comparison of the methods and the results obtained. PDI provides a spanwise averaged instantaneous quantitative flow field picture whereas LDV yields a long time averaged point measurement of the flow. The Mach numbers derived from both methods are compared in Fig. 17(Ref. 14) at  $\alpha = 10^\circ$ , when the airfoil is undergoing downward motion. The solid lines shown in it are the Mach number contours corresponding to the centerline of the dark fringes in the interferograms and the dashed lines are the Mach number contours obtained from LDV (plotted for the corresponding fringe numbers). The agreement is good, considering the vastly different nature of the techniques. The cylinder of light used in PDI provides data points closer to the airfoil surface, which was not possible with LDV because of the blockage of the beams by the oscillating airfoil. However, the agreement for those data that are coincident

demonstrates the statistically stationary nature of the partially separated flow field in the region compared. It should be noted that major differences could appear in separated flow regions or in three dimensional flows.

Since LDV is a point measurement whose resolution is controllable, very detailed surveys of the flow could be obtained. The resolution of PDI is limited to the number of fringes that naturally form based on the laser wavelength, the wind tunnel span and the flow density changes. But, PDI offers flow field information instantaneously, obtaining this information would be a very time consuming task with LDV, a major consideration in high speed, forced, unsteady flows. The agreement obtained in this study enhances the confidence level of the results presented.

#### **4.B.3. Flow Description from PDI and LDV Studies: Untripped**

**Airfoil;  $\alpha = 10^\circ - 2^\circ \sin \omega t$**

The key factors characterizing large amplitude dynamic stall discussed above flow are the large scale flow separation and the origination of the dynamic stall vortex in the vicinity of/during the bursting of the laminar separation bubble. Attempts at modelling the flow have not been very successful, since a satisfactory turbulence model for this flow is still unavailable. Neither fully laminar nor fully turbulent computations have yielded results matching the experiment. It is thus imperative that successful modeling of the flow requires inclusion of the role of transition in the dynamic stall process. For this purpose, it was felt that low amplitude oscillatory motion very near the static stall angle offers a better test case than the large amplitude problem. Hence, more experiments were conducted for the case of  $\alpha = 10^\circ - 2^\circ \sin \omega t$ . Some typical results will be discussed below.

##### **4.B.3.A. PDI Studies**

PDI images (Fig. 18a -18f) were obtained at  $M = 0.3$  and  $k = 0.05$ , throughout the oscillation cycle. Fig. 18a shows that at  $\alpha = 8.0^\circ$ , a laminar separation bubble exists on the airfoil surface. The flow does not show marked changes as the airfoil is pitched up to  $\alpha = 12.0^\circ$ . Slight variations in the flow underneath the bubble can be seen. The static

stall angle at  $M = 0.3$  was determined to be 12.4 deg. Thus, the airfoil always remained below the static stall angle. On the downstroke, Fig. 18d shows that at  $\alpha = 11.5^\circ$ , the flow has actually separated at an angle of attack *less than* the static stall angle. At  $\alpha = 10.5^\circ$  on the downstroke, the flow has once again reattached and the bubble has reformed at  $\alpha = 9.0^\circ$ . This behavior was indeed unexpected. It is clear that the vorticity input by the unsteady motion has to be shed through the boundary layer in which case, the flow adjusts instantaneously to each angle of attack throughout the cycle. But, if there is a mismatch in the time scales of unsteady motion and the rate of vorticity diffusion in the boundary layer this vorticity must be abruptly shed by convection at lower than static stall angle of attack when the angle of attack is decreasing. More details of the flow and some comparisons with computations of the problem which were obtained by using empirical models for transition onset and length are provided in Ref. 18.

#### 4.B.3.B. LDV Studies

Detailed LDV measurements were also obtained prior to PDI experiments. The results are reported in Ref. 19. A first look at the velocity data for the 2 deg. amplitude flow at  $M = 0.3$  and  $k = 0.05$  indicated that a bubble formed, but the velocity profiles could not confirm the bursting of the bubble. It was thought that the bubble simply changed shape during the cycle and did not burst since the maximum angle of attack reached during the oscillation cycle was less than the static stall angle of 12.4 deg. However, comparison of vorticity distributions obtained as explained earlier showed that at  $\alpha = 11.53^\circ$ , Fig. 19a, the peak clockwise vorticity level was about -40 units near the leading edge. But, as shown in Fig. 19b, at an angle of attack of 11.0 deg. the maximum clockwise vorticity dropped rapidly to -25 units. As the angle of attack was further reduced to 10.0 deg., (not shown) the peak vorticity increased again pointing to the occurrence of light dynamic stall at  $\alpha = 11.0^\circ$  in the low amplitude case. The good agreement between PDI and LDV results reaffirms the above inferences. The computation of the flow has proceeded using the LDV data to qualify the computed velocity distributions and the PDI data to qualify the computed global pressure field<sup>20</sup>.

#### 4.B.4. Tripped Airfoil Studies: Role of Transition in Large Amplitude Dynamic Stall

As stated earlier, the dynamic stall vortex forms near the point where the separating shear layer undergoes transition. Thus, it can be expected that factors affecting transition also affect the processes of dynamic stall onset and vortex formation. Applicability of low Reynolds number testing methods and test data to model rotors and eventually to flight Reynolds numbers thus becomes a formidable challenge and suffers from several limitations. Whereas this situation is not new, it is nevertheless a major issue in model rotor testing, since the process of flow separation is particularly sensitive to the state of the boundary layer. A standard approach to simulate high Reynolds number results in the laboratory is to conduct tests by tripping the airfoil boundary layer with the intent that the flow subsequently develops as a fully turbulent flow. It is important to recognize that despite the vast number of previous experimental studies on tripping in steady flow and the recommendations on the right kind of trips that have resulted, these schemes are not directly applicable to dynamic stall flow; and the use of steady flow tripping schemes for dynamic stall flow studies has not been satisfactory. With these limitations in mind, the airfoil was tripped as described in Sec. 4.A.2.3. After analyzing the data, it was found that trip 4 was the most satisfactory. Some pertinent results will be presented below and the results for all the trips can be found in Ref. 6.

##### 4.B.4.A. Qualitative Analysis

Figures 20a and 20b (Ref. 6) compare interferograms over the airfoil without and with the optimum trip at  $M = 0.3$  and  $k = 0.05$  and  $\alpha = 10.0^\circ$ . The presence of the laminar bubble can be clearly found in Fig. 20a by studying the fringe pattern. In Fig. 20b, the fringe very near the airfoil leading edge shows a closed loop pattern, which corresponds to a well defined suction peak. The fringes slightly downstream of the suction peak meet the upper surface over a small length of the airfoil region rather than near a point as seen in Fig. 20a. This fringe pattern indicates the absence of the bubble; the corresponding pressure distributions confirmed this interpretation (Ref. 6). Fig. 20c shows the flow field

at  $\alpha = 13.99^\circ$  when the dynamic stall vortex has fully formed and has convected past the  $x/c = 0.25$  point for the untripped airfoil, whereas in Fig. 20d, at the same angle of attack, the vertical fringes which precede the dynamic stall vortex have just appeared, pointing very definitely to delay of stall that was achieved due to the presence of the trip, (it is worth pointing that if improper trips were used, the stall process could actually be accelerated, as was demonstrated in Ref. 9).

#### 4.B.4.B Quantitative Analysis

Figures 21a and 21b present the variation of the airfoil peak suction pressure coefficient in the presence of the trip at  $M = 0.3$  and  $M = 0.45$  respectively for  $k = 0.05$ . The significantly increased suction levels are proof that the airfoil was tripped successfully and a flow more representative of turbulent flow dynamic stall was achieved in the wind tunnel. It is interesting to note that in Fig. 21b, the  $C_{p_{min}}$  values for both the untripped and tripped airfoil exceed the critical value of  $-2.76$ ; thus, the flow in both cases becomes supersonic. The larger  $C_p$  values of the tripped airfoil flow suggest that the local Mach numbers in this flow are higher. It is interesting to note that despite the larger Mach number, the shock system that results over the airfoil is much less dramatic and only two shocks can be seen in the pressure distribution in Fig. 22 for  $M = 0.45$ ,  $k = 0.05$  and  $\alpha = 10.0^\circ$  (compared to Fig. 11 for the untripped airfoil) which can be attributed to the flow being more turbulent over it. Also, it is seen that the local  $C_p$  values are higher and the extent of the sonic line is much wider over the airfoil. Its shape is also different, with a bulging front and a longer tail extending to  $x/c = 0.15$ . Further, there is no flow separation seen in this case.

Fig. 23 compares the pressure distributions over the front portion of the airfoil for the untripped and tripped flows. Also plotted are the  $C_p$  values of Carr et al<sup>21</sup> obtained at a higher Reynolds number of  $3 \times 10^6$ . It is clear that tripping helped the elimination of the bubble and also produce a slightly higher suction pressure, but the peak suction is still short of the higher Reynolds number data. Some of the difference is attributable to the loss of momentum due to the presence of the trip. This is one of the limitations of any

tripping study.

#### 4.B.5. Role of Adverse Pressure Gradient

The most important factor governing flow separation is the adverse pressure gradient in the flow, if there are no shock induced effects. As was seen earlier, the mere presence of a shock does not always cause separation. It has been shown <sup>22</sup> that the shock has to attain certain strength before it can actually induce separation. Thus, it would be educative to study the local adverse pressure gradient in the dynamic stall flow near the vortex formation location. Since this point is not very clear, the adverse pressure gradient following the suction peak was studied. For the laminar boundary layer to separate, the pressure gradient has to reach a certain value. However, its transition enables reattachment and the flow can withstand higher values of  $(\frac{dC_p}{d(x/c)})$ . At high angles of attack, the laminar shear layer *fails* to reattach, causing dynamic stall to occur. It has been shown in Ref. 9 that dynamic stall is initiated over a transiently pitching airfoil when the leading edge adverse pressure gradient  $(\frac{dC_p}{d(x/c)})$  reaches a critical value that depends upon Mach number and pitch rate. Fig. 24 shows that for a transiently pitching airfoil, **the critical adverse pressure gradient decreases with increasing Mach number**. This is in fact the effect of compressibility on dynamic stall. It appears that **compressibility weakens the ability of the boundary layer to withstand the adverse pressure gradient, even though the adverse pressure gradient itself is smaller**. Since vorticity flux is related to adverse pressure gradient, it appears that the vorticity in the local compressible boundary layer coalesces at lower levels than in incompressible flow at any given pitch rate. Increasing the pitch rate increases the vorticity input to the boundary layer, which seems to enable the boundary layer to withstand higher levels of adverse pressure gradients, (Fig. 10, Ref. 12). Yet, the levels achieved in the compressible cases appear to be considerably smaller than those seen in incompressible flow. This result seems to be true for both the untripped and tripped airfoils.

Figure 25 presents the adverse pressure gradient development over the oscillating airfoil at  $M = 0.3$  at  $k = 0.05$ . For the untripped airfoil, the pressure gradient immediately

following the suction peak is plotted. It was found that the value of the pressure gradient at the formation of the laminar separation bubble is about 40, at an angle of attack of about 7 deg. Dynamic stall is seen to occur at a pressure gradient of 125 at  $\alpha = 12.5^\circ$ . As the dynamic stall vortex begins to convect, the pressure gradient drops. In case of the tripped airfoil, the dynamic stall process begins at  $\alpha = 13.5^\circ$ , when the pressure gradient is about 150. Thus, there is a slight delay of stall, attributable to an improvement in the ability of the boundary layer to withstand the forces inducing flow separation. The trends at other reduced frequencies were nearly the same, although at times the pressure gradients near dynamic stall vortex formation angle of attack were slightly less for the tripped airfoil when compared to the untripped flow. But, the values were *always* higher than that at which the laminar separation bubble formed in the untripped flow. Some of the differences seen can be attributed to the noise inherent in the process of numerical differentiation of the airfoil surface pressure distribution to obtain the pressure gradient information. Also, any trip, however small it is, still increases the momentum thickness of the boundary layer and hence, introduces additional drag, which has the equivalent effect of reducing the total adverse pressure gradient that can be attained before stall occurs. This points to the difficulty of conducting laboratory tests by tripping to simulate the higher Reynolds number flow, a fact of critical importance to model rotor testing.

#### 4.B.6. Conclusions

The major results from a four year study of the effects of compressibility on dynamic stall of oscillating airfoils have been reported. The flow was studied using stroboscopic point diffraction interferometry(PDI) and unsteady LDV techniques. The former was developed for use in unsteady separated flows to provide a quantitative description of the instantaneous surface and global pressure distributions of the flow. The experimental conditions were chosen to be directly relevant to that of a helicopter model rotor retreating blade. The results show that the process of dynamic stall vortex formation occurs rapidly in a very small (half-a-degree) angle of attack range. Compressibility effects become critical at a free stream Mach number of 0.3. Compressibility promotes dynamic stall onset by

decreasing the angle of attack at which the flow separates with increasing in Mach number. The strongly compressible local flow can produce multiple shocks in the leading edge region, and at times can also induce flow separation leading to dynamic stall. As much as two degrees of stall onset delay was observed at  $M = 0.3$  when compared to steady flow. The PDI results also revealed that dynamic stall occurred as the laminar separation bubble that formed over the airfoil broke down. Evidence points to the failure of the laminar shear layer to reattach as the cause of stall onset. The premature stall at higher Mach numbers could be attributed to the inability of the compressible boundary layer to withstand the adverse pressure gradient in the flow leading to a rapid coalescence of vorticity. Increasing unsteadiness has a beneficial effect in this regard, even in compressible flow. A separation bubble forms when the flow reattaches as well. The reattachment process extends to about four degrees below the static stall angle for the case studied causing a large hysteresis loop. Tests conducted to simulate higher Reynolds number flow situations by tripping the leading edge boundary layer have revealed some of the issues and concerns of tripping leading-edge-stalling flows.

A case of light dynamic stall was encountered when oscillating the airfoil at low amplitudes with maximum angle of attack less than the static stall angle. This was attributed to the differences in time scales of vorticity diffusion through the boundary layer and that of the imposed unsteadiness.

The various fluid flow physics issues that have been uncovered by this investigation include formation of multiple shocks, effects of leading edge pressure gradient in unsteady flow separation as affected by the degree of unsteadiness, the progressive lag in the leading edge pressure development with increase in pitch rate, and the effects of boundary layer transition. The quantitative flow field data base that has been developed will be of significant value to researchers involved in flow modelling and in validating CFD codes developed to represent this complex and challenging flow phenomenon.

The implication of the results to dynamic stall control is that onset of compressibility effects, when not possible to avoid, should at least be delayed. Since vorticity is shed in light stall case also, it is important that the control scheme be able to modify the vorticity field by either diffusing it rapidly or by removing it from near the airfoil. If

“incompressible” flow can be maintained over the airfoil leading edge for different flow conditions, then considerable delay in dynamic stall can be achieved.

#### 4.C. LIST OF PUBLICATIONS AND TECHNICAL REPORTS

1. S.Ahmed and M.S.Chandrasekhara, "Reattachment Studies of an Oscillating Airfoil Dynamic Stall Flow Field", (AIAA Paper 91-3225), *AIAA Journal*, Vol. 32, No. 5, May 1994, pp. 1006 - 1012.
2. L.W.Carr, M.S.Chandrasekhara and N.Brock, "A Quantitative Study of Unsteady Compressible Flow on an Oscillating Airfoil", (AIAA Paper 91-1683), *Journal of Aircraft*, Vol. 31, No. 4, Jul. - Aug. 1994, pp. 892 - 898.
3. L.W.Carr, M.S.Chandrasekhara, S.Ahmed and N.Brock, "A Study of Dynamic Stall Using Real-Time Interferometry", (AIAA Paper 91-0007), *Journal of Aircraft*, Vol. 31, No. 4, Jul. - Aug. 1994, pp. 991 - 993.
4. M.S.Chandrasekhara and S.Ahmed, "Velocity and Vorticity Distributions Over an Oscillating Airfoil Under Compressibility Conditions", *AIAA Journal*, Vol. 31, No. 6, June 1993, pp. 995-996.
5. L.W.Carr and M.S.Chandrasekhara, "Compressibility Effects on Dynamic Stall", **Invited Paper** under preparation for *Progress in Aerospace Sciences*.
6. R.A.Hess, N.J.Brock, L.W.Carr, and M.S.Chandrasekhara, "A Holographic Animation of Compressible Flow Interferograms", **Prize Winning Entry** in "Gallery of Fluid Motion", *Physics of Fluids*, Vol. 4, No. 9, Sep. 1992, pp. 1869 - 1882.
7. L.W.Carr, and M.S.Chandrasekhara, "A Study of Compressibility Effects on Dynamic Stall of Rapidly Pitching Airfoils", *Computer Physics Communications*, Elsevier Science Publishers, B.V., Vol. 65 (1991), pp. 62-68.
8. M.S.Chandrasekhara and L.W.Carr, "Compressibility Effects on Dynamic Stall of Oscillating Airfoils", *AGARD-CP-552, Proc. of the AGARD 75<sup>th</sup> Fluid Dynamics Panel Meeting on Aerodynamics and Aeroacoustics of Helicopters*, pp. 3.1 - 3.15, Berlin, October 10-13, 1994.
9. M.S.Chandrasekhara, M.C.Wilder and L.W.Carr, "Boundary Layer Tripping Studies

- of Compressible Dynamic Stall Flow", *AIAA Paper No. 94-2340*, 25<sup>th</sup> Fluid Dynamics Conference, Colorado Springs, Co, June 20-23, 1994.
10. R.D.VanDyken, J.A.Ekaterinaris, M.S.Chandrasekhara and M.F.Platzer, "Analysis of Compressible Steady and Oscillatory Airfoil Flows at Transitional Reynolds Numbers", *AIAA Paper No. 94-2225*, 25<sup>th</sup> Fluid Dynamics Conference, Colorado Springs, Co, June 20-23, 1994.
  11. J.A.Ekaterinaris, M.S.Chandrasekhara and M.F.Platzer, "Analysis of Low Reynolds Number of Airfoil Flows", *AIAA Paper No. 94-0534*, 32<sup>nd</sup> Aerospace Sciences Meeting, Jan. 10-13, 1993, Reno, NV.
  12. M.S.Chandrasekhara and R.D.VanDyken, "LDV Measurements in Dynamically Separated Flows", *Proc. of the Fifth International Conference on Laser Anemometry - Advances and Applications*, Koningshof, The Netherlands, Aug. 1993, *SPIE Vol. 2052*, pp. 305-312.
  13. Y.C.Cho, L.W.Carr and M.S.Chandrasekhara, "Corrections to Fringe Distortion due to Flow Density Gradients in Optical Interferometry", *AIAA Paper 93-0631*, 31<sup>st</sup> Aerospace Sciences Meeting, Reno, NV, Jan. 11-14, 1993.
  14. M.S.Chandrasekhara, "Oscillating Airfoil Compressible Dynamic Stall Studies", **Invited Paper** *Proc. of the I.I.Sc. International Symposium on Advances in Aerospace Sciences and Engineering*, Interline Publishing, Bangalore, India, December 1992, Vol.1, pp. 115-123.
  15. M.S.Chandrasekhara, L.W.Carr, and J.A.Ekaterinaris, "Interferometry and Computational Studies of an Oscillating Airfoil Compressible Dynamic Stall", in *Proc. of the 5<sup>th</sup> Asian Congress of Fluid Mechanics*, Taejon City, Korea, Aug. 1992, Vol. II, pp. 1047 - 1050.
  16. R.D.Vandyken and M.S.Chandrasekhara. "Leading Edge Velocity Field of an Oscillating Airfoil in Compressible Dynamic Stall", *AIAA Paper 92 - 0193*, 30<sup>th</sup> Aerospace Sciences Meeting, Jan. 6 - 9, 1992, Reno, NV.

17. M.S.Chandrasekhara and R.D.VanDyken, "Velocity Measurements Around the Leading Edge of an Oscillating Airfoil Experiencing Dynamic Stall", *Proc. the 8<sup>th</sup> Symposium on Turbulent Shear Flows*, München, Germany, Sep. 1991, Vol. 2, pp. I.3.1 - I.3.2.
18. M.S.Chandrasekhara and S.Ahmed, "Laser Velocimetry Measurements of Oscillating Airfoil Dynamic Stall Flow Field", *AIAA Paper 91-1799*, 22<sup>nd</sup> Fluid Dynamics, Plasma Dynamics and Lasers Conference, June 24-26, 1991, Honolulu, HI.
19. L.W.Carr, M.S.Chandrasekhara and S.Ahmed, "Impact of Compressibility on Boundary Layer Environment of Dynamically Stalling Airfoils", *EUROMECH 272 Colloquium on Response of Shear Flows to Imposed Unsteadiness*, Aussois, France, January 1991.

#### Papers Published with Partial ARO Support

1. M.S.Chandrasekhara, D.D.Squires, M.C.Wilder and L.W.Carr, "A Phase-Locked High-Speed Real-Time Interferometry System for Large Amplitude Unsteady Flows", *Proc. 7<sup>th</sup> International Symposium on Applications of Laser Techniques to Fluid Mechanics*, July 1994, Lisbon, Portugal, pp. 38.3.1-38.3.8.
2. M.S.Chandrasekhara, L.W.Carr and M.C.Wilder, "Interferometric Investigations of Compressible Dynamic Stall Over a Transiently Pitching Airfoil", (AIAA Paper 93-0211), *AIAA Journal*, Vol. 32, No. 3, March 1994, pp. 586-593.
3. M.S.Chandrasekhara, M.C.Wilder and L.W.Carr, "Transition Effects on Compressible Dynamic Stall of Transiently Pitching Airfoils", *AIAA Paper 93-2978 24<sup>th</sup> Fluid Dynamics Conference*, Orlando, FL, July 6-9, 1993.
4. M.F.Platzer, M.S.Chandrasekhara, J.A.Ekaterinaris and L.W.Carr, "Dynamic Airfoil Investigations", *Proc. of the 5<sup>th</sup> Symposium on Numerical and Physical Aspects of Aerodynamic Flows*, Jan. 1992, Long Beach, CA.
5. M.S.Chandrasekhara, L.W.Carr and S.Ahmed, "Comparison of Pitch Rate History

Effects on Dynamic Stall", *Proc. of NASA/AFOSR/ARO Workshop on Physics of Forced Unsteady Separation*, NASA CP 3144, pp. 23-34, 1992

6. N.Brock, M.S.Chandrasekhara and L.W.Carr, "A Real Time Interferometry System for Unsteady Flow Measurements", *ICIASF'91 RECORD, IEEE Publication 91CH3028-8*, pp. 423-430.

#### 4.D. LIST OF ALL PARTICIPATING PERSONNEL

1. Professor M.S.Chandrasekhara, NPS, Monterey, CA
2. Professor M.F.Platzer, NPS, Monterey, CA
3. Professor J.A.Ekaterinaris, NPS, Monterey, CA
4. Mr. R.D.VanDyken, Ph.D. Student, NPS, Monterey, CA
5. Dr. L.W.Carr, Cooperative participant, Group Leader, U.S. Army AFDD, ATCOM, Moffett Field, CA
6. Dr. Y.C.Cho, Cooperative participant, Scientist, NASA ARC
7. Dr. M.C.Wilder, Scientist, MCAT Instt.
8. Dr. S.Ahmed, Scientist, MCAT Instt.
9. Mr. D.D.Squires, Engineer, Sverdrup Tech., Inc.
10. Mr. N.J.Brock, Scientist, Aerometrics, Inc.
11. Mr. R.A.Hess, Scientist, Aerometrics, Inc.

#### 5. REPORT OF INVENTIONS

NONE.

## 6. BIBLIOGRAPHY

1. Carr, L.W. and Chandrasekhara, M.S., "Design and Development of a Compressible Dynamic Stall Facility", *Journal of Aircraft*, **29**, 3, May-June 1992, pp. 314-318.
2. Brock, N., Chandrasekhara, M.S. and Carr, L.W., "A Real Time Interferometry System for Unsteady Flow Measurements", *ICIASF'91 RECORD*, IEEE Publication **91CH3028-8**, pp. 423-430.
3. Cho, Y.C., Carr, L.W., and Chandrasekhara, M.S., "Corrections to Fringe Distortion due to Flow Density Gradients in Optical Interferometry", *AIAA Paper 93-0631*, 31<sup>st</sup> Aerospace Sciences Meeting, Reno, NV, Jan. 11-14, 1993.
4. Chandrasekhara, M.S., and Ahmed, S., "Laser Velocimetry Measurements of Oscillating Airfoil Dynamic Stall Flow Field," *AIAA Paper 91-1799*, Presented at the 22<sup>nd</sup> Fluid Dynamics, Plasma Dynamics and Lasers Conference, Honolulu, HI, June 24-26, 1991.
5. Chandrasekhara, M.S., Squires, D.D, Wilder, M.C., and Carr, L.W., "A Phase-Locked High-Speed Real-Time Interferometry System for Large Amplitude Unsteady Flows", *Proc. 7<sup>th</sup> International Symposium on Applications of Laser Techniques to Fluid Mechanics*, July 1994, Lisbon, Portugal, pp. 38.3.1-38.3.8.
6. Chandrasekhara, M.S., Wilder, M.C. and Carr, L.W., "Boundary Layer Tripping Studies of Compressible Dynamic Stall Flow", *AIAA Paper No. 94-2340*, 25<sup>th</sup> Fluid Dynamics Conference, Colorado Springs, Co, June 20-23, 1994.
7. Nakamura, Y., and Tomonari, Y., "The Effects of Roughness on the Flow Past Circular Cylinders at High Reynolds Numbers", *Journal of Fluid Mechanics*, **123**, 1982, pp. 363-378.
8. Pope, A., and Goin, K.L., *High Speed Wind Tunnel Testing*, Kraeger Publishing Company, New York, NY, 1978.
9. Wilder, M.C., Chandrasekhara, M.S., and Carr, L.W., "Transition Effects on the Compressible Dynamic Stall of Transiently Pitching Airfoil", *AIAA Paper No. 93-2978*, 24<sup>th</sup> Fluid Dynamics Conference, Orlando, FL, July 6 -9, 1993.

10. Carr, L.W., Chandrasekhara, M.S. and Brock, N.J., "A Quantitative Visual Study of Unsteady Compressible Flow on an Oscillating Airfoil", *Journal of Aircraft*, **31**, No. 4, pp. 892-898.
11. Carr, L.W., Chandrasekhara, M.S., Ahmed, S., and Brock, N.J., "A Study of Dynamic Stall Using Real Time Interferometry," *Journal of Aircraft*, **31**, No. 4, pp. 991-993.
12. Chandrasekhara, M.S., and Carr, L.W., "Compressibility Effects on Dynamic Stall of Oscillating Airfoils", *AGARD-CP-552*, Oct. 1994, pp. 3.1 - 3.15.
13. Chandrasekhara, M.S., Carr, L.W., and Wilder, M.C., "Interferometric Investigations of Compressible Dynamic Stall Over a Transiently Pitching Airfoil", *AIAA Journal*, **31**, No.3, Mar. 1994, pp. 586-593.
14. Ahmed, S., and Chandrasekhara, M.S., "Reattachment Studies of an Oscillating Airfoil Dynamic Stall Flow Field", *AIAA Journal*, **31**, No. 5, May 1993, pp. 1006-1012.
15. Chandrasekhara, M.S., and VanDyken, R.D., "LDV Measurements in Dynamically Separated Flows", *Proc. of the Fifth International Conference on Laser Anemometry - Advances and Applications*, Koningshof, The Netherlands, Aug. 1993, **SPIE Vol. 2052**, pp. 305-312.
16. Chandrasekhara, M.S. and Carr, L.W. "Flow Visualization Studies of the Mach Number Effects on the Dynamic Stall of Oscillating Airfoils", *Journal of Aircraft*, **27**,6, June 1990, pp. 516-522.
17. Chandrasekhara, M.S., and Ahmed, S., "Velocity and Vorticity Distributions Over an Oscillating Airfoil Under Compressibility Conditions", *AIAA Journal*, **30**, No. 6, June 1993, pp. 995-996.
18. Van Dyken, R.D., "A Study of Low Reynolds Number Dynamic Stall", *Ph.D. Thesis*, Dept. of Aeronautics and Astronautics, U.S. Naval Postgraduate School, Monterey, CA, June. 1995.
19. Vandyken, R.D., and Chandrasekhara, M.S., "Leading Edge Velocity Field of an Oscillating Airfoil in Compressible Dynamic Stall", *AIAA Paper 92-0193*, 30<sup>th</sup> Aerospace Sciences Meeting, Jan. 6-9, 1992, Reno, NV.

21. VanDyken, R.D., Ekaterinaris, J.A., Chandrasekhara M.S., and Platzer, M.F., "Analysis of Compressible Steady and Oscillatory Airfoil Flows at Transitional Reynolds Numbers", *AIAA Paper No. 94-2225*, 25<sup>th</sup> Fluid Dynamics Conference, Colorado Springs, Co, June 20-23, 1994.
21. Carr, L.W., McAlister, K.W. and McCroskey, W.J., "Analysis of Development of Dynamic Stall Based on Oscillating Airfoil Experiments", **NASA TN D-8382**, 1977.
22. Pearcey, H.H., "Some Effects of Shock-Induced Separation of Turbulent Boundary-Layers in Transonic Flow Past Airfoils", *Proc. Symposium on Boundary Layer Effects in Aerodynamics*, Paper 9, National Physics Laboratory, Great Britain, 1955, pp. 1-84.

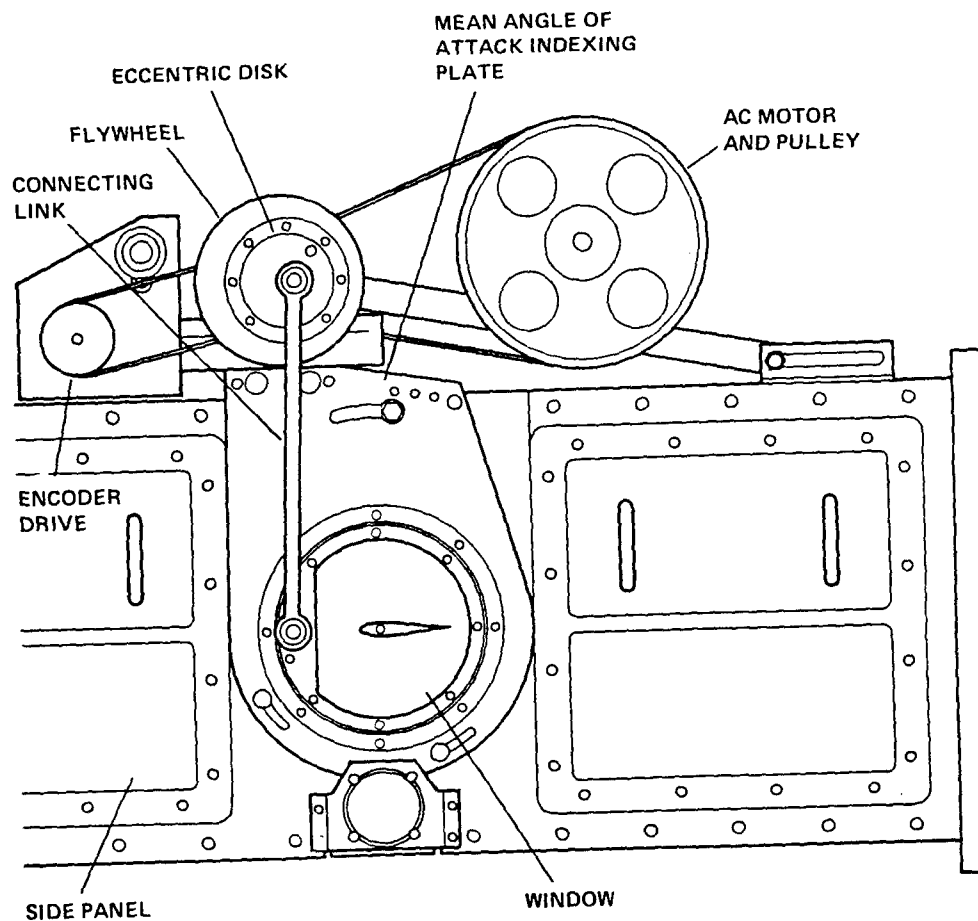


Fig. 1. Side View of the Compressible Dynamic Stall Facility

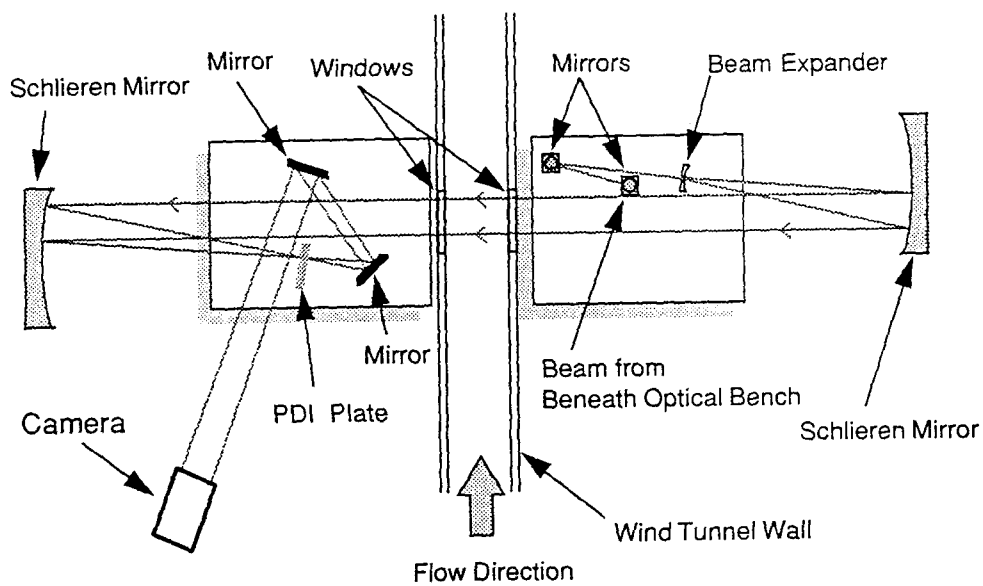


Fig. 2. Schematic of the Point Diffraction System

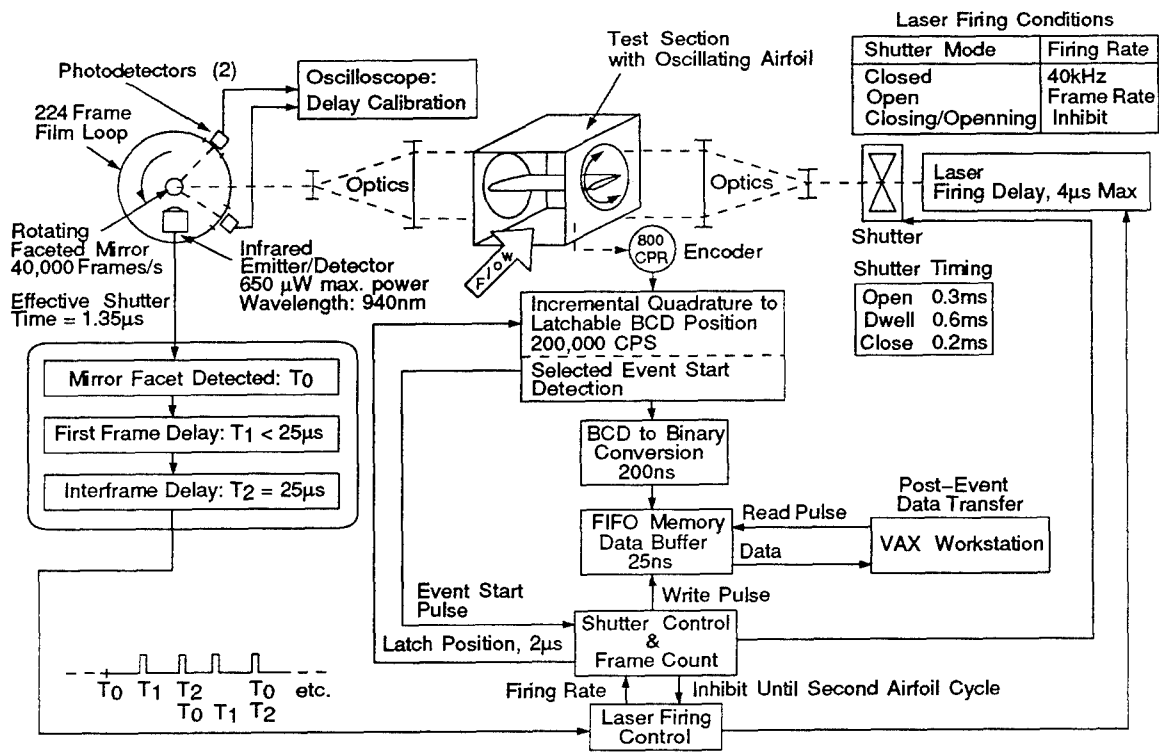


Fig. 3. Schematic of Camera/Laser Synchronization for the High-Speed Phase-Locked Interferometry Imaging System

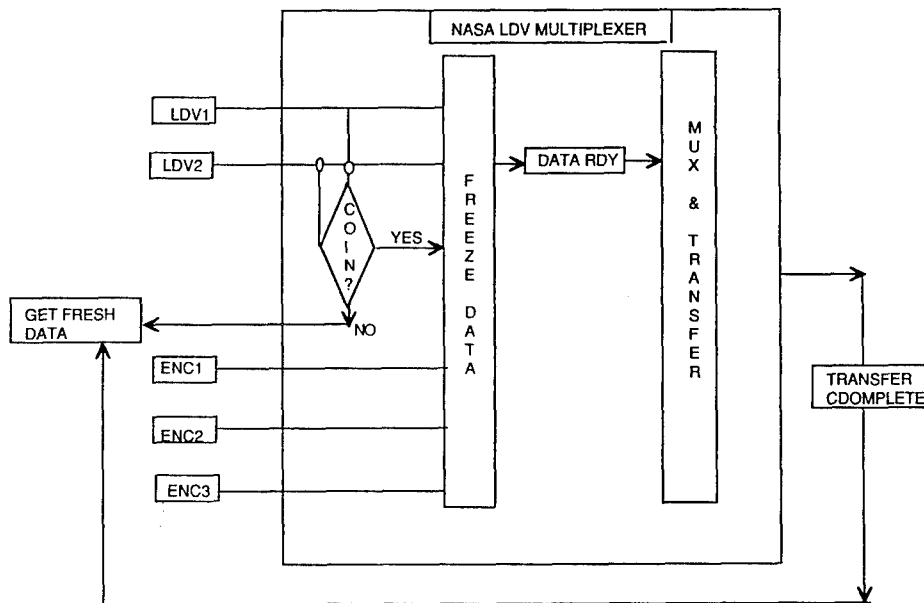
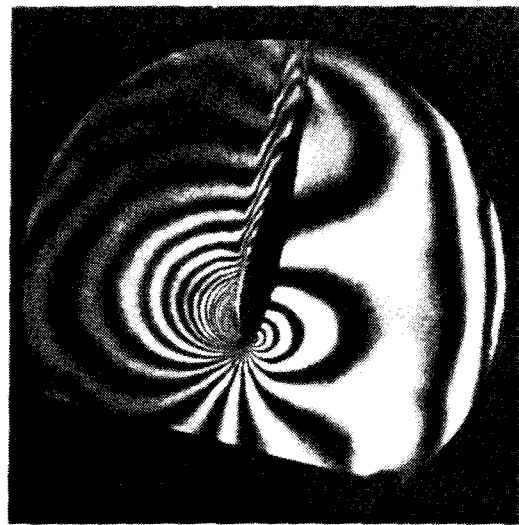
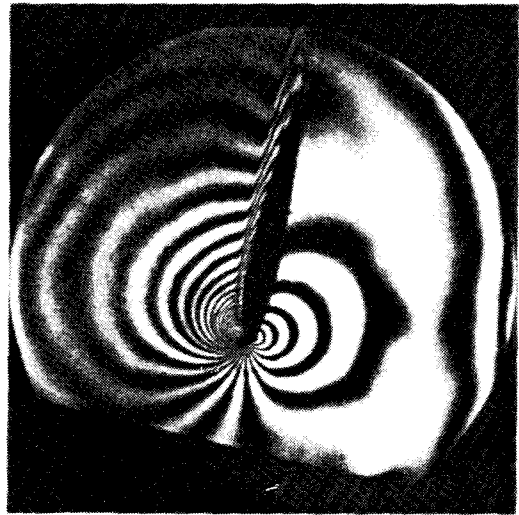


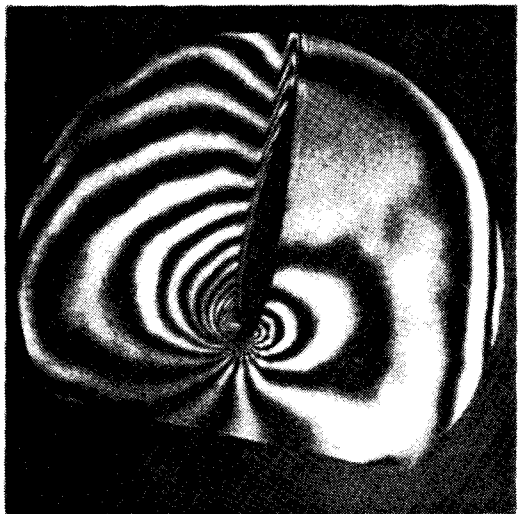
Fig. 4. Schematic of the Unsteady Flow LDV Data Acquisition Method



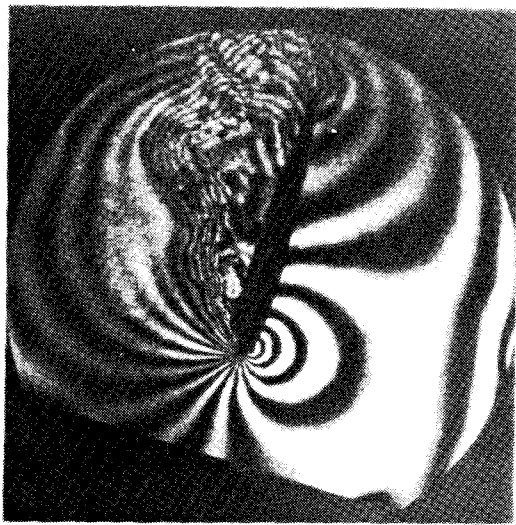
(c)  $\alpha = 12.54^\circ$



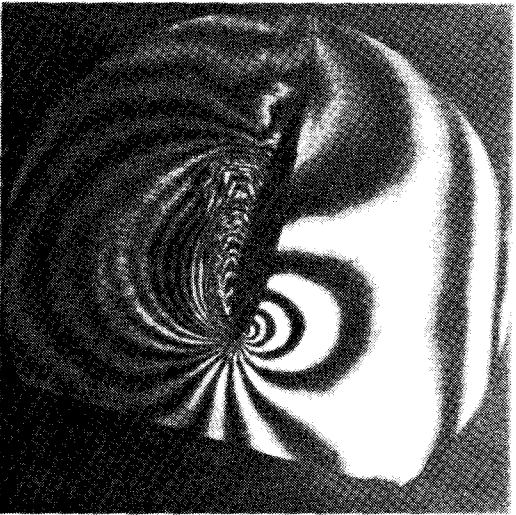
(b)  $\alpha = 12.11^\circ$



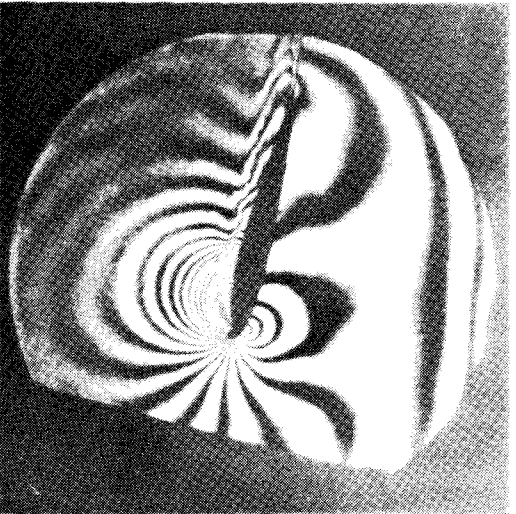
(a)  $\alpha = 10.65^\circ$



(f)  $\alpha = 16.02^\circ$



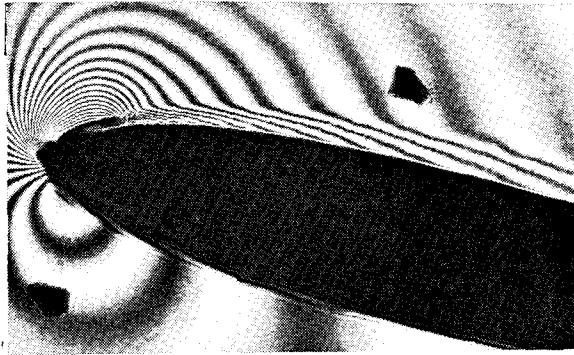
(e)  $\alpha = 13.85^\circ$



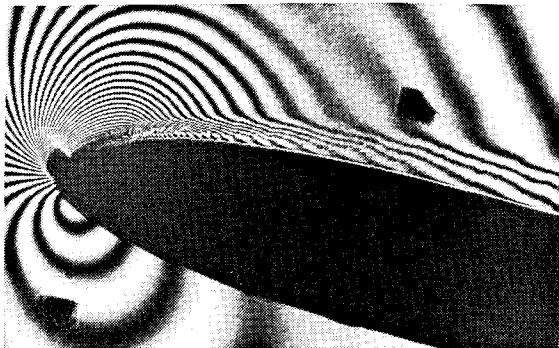
(d)  $\alpha = 12.83^\circ$

Fig. 5. Interferogram Sequence of Dynamic Stall Development Over an Oscillating Airfoil:  $M = 0.35$ ,  $k = 0.05$

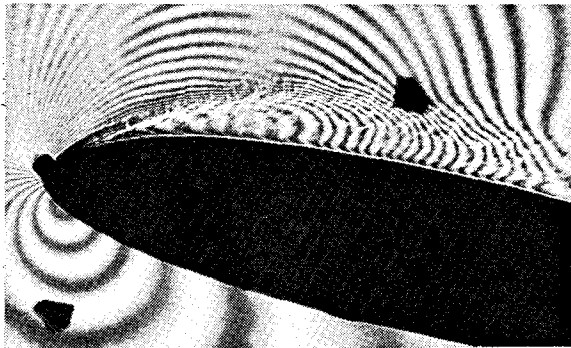
(a)  $M = 0.3$



(b)  $M = 0.35$



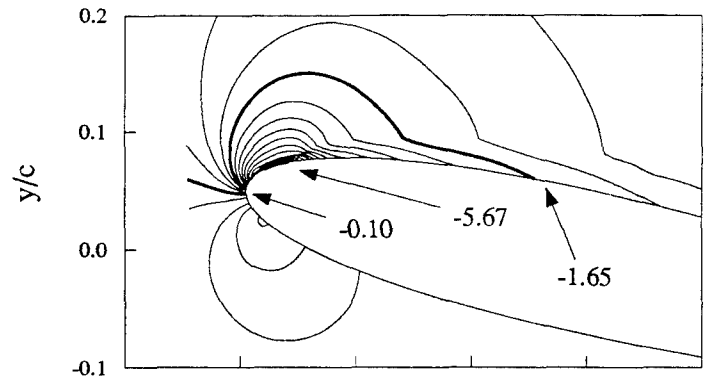
(c)  $M = 0.4$



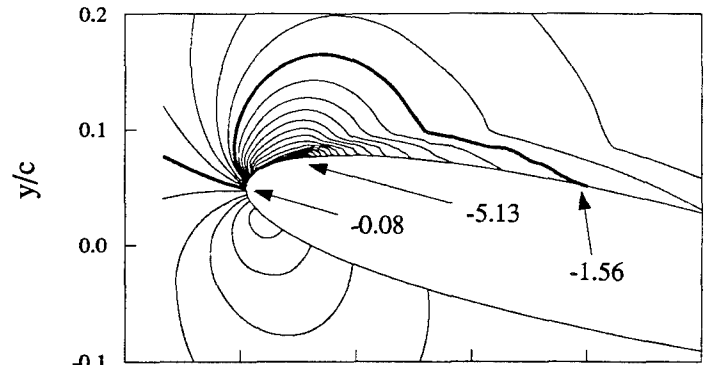
(d)  $M = 0.45$



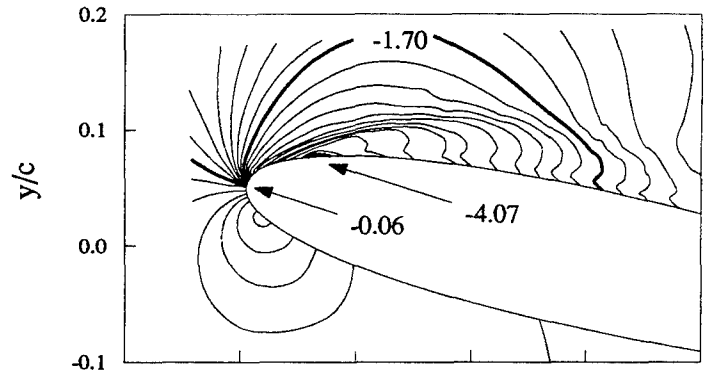
(e)  $M = 0.3$



(f)  $M = 0.35$



(g)  $M = 0.4$



(h)  $M = 0.45$

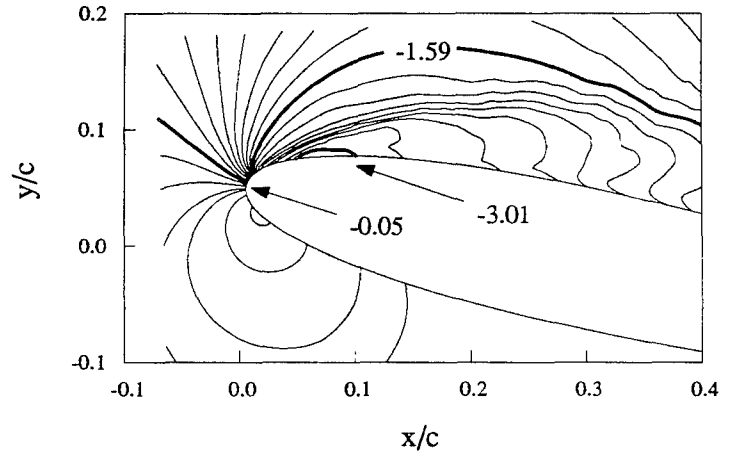


Fig. 6. Effect of Mach Number on Dynamic Stall: (a-d) PDI Images; (e-h) Global Pressure Fields

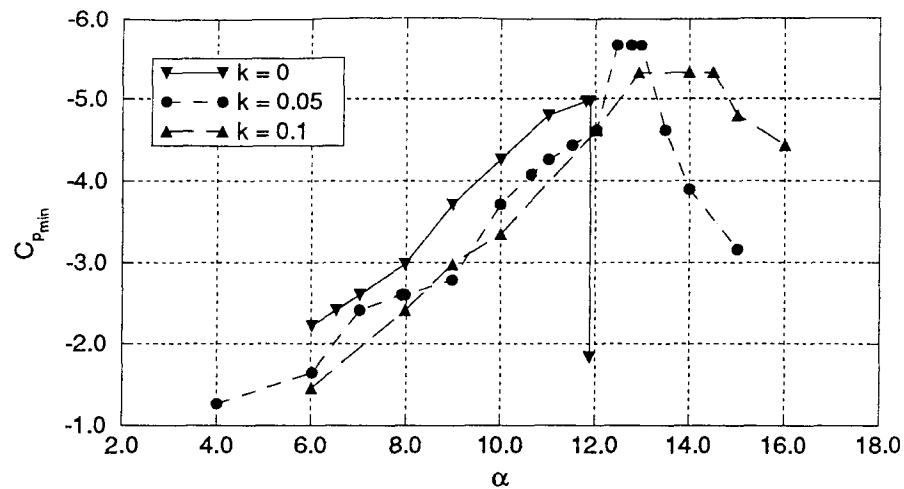


Fig. 7. Effect of Unsteadiness on Airfoil Peak Suction Development:  $M = 0.3$

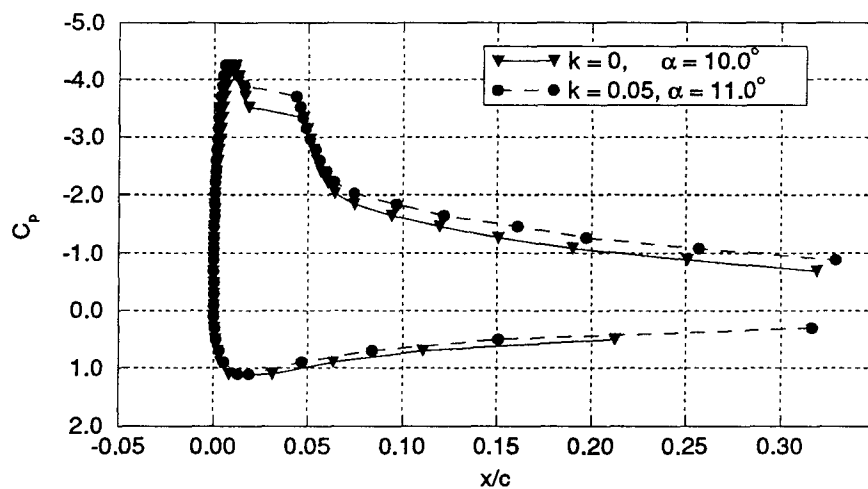


Fig. 8. Comparison of Steady and Unsteady Airfoil Pressure Distributions:  $M = 0.3$

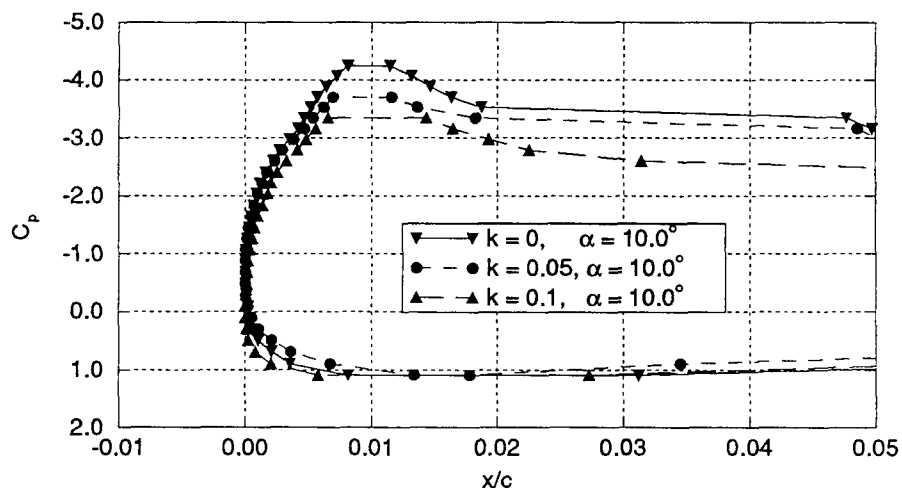


Fig. 9. Effect of Unsteadiness on Airfoil Leading Edge Pressure Distribution:  $M = 0.3$ .

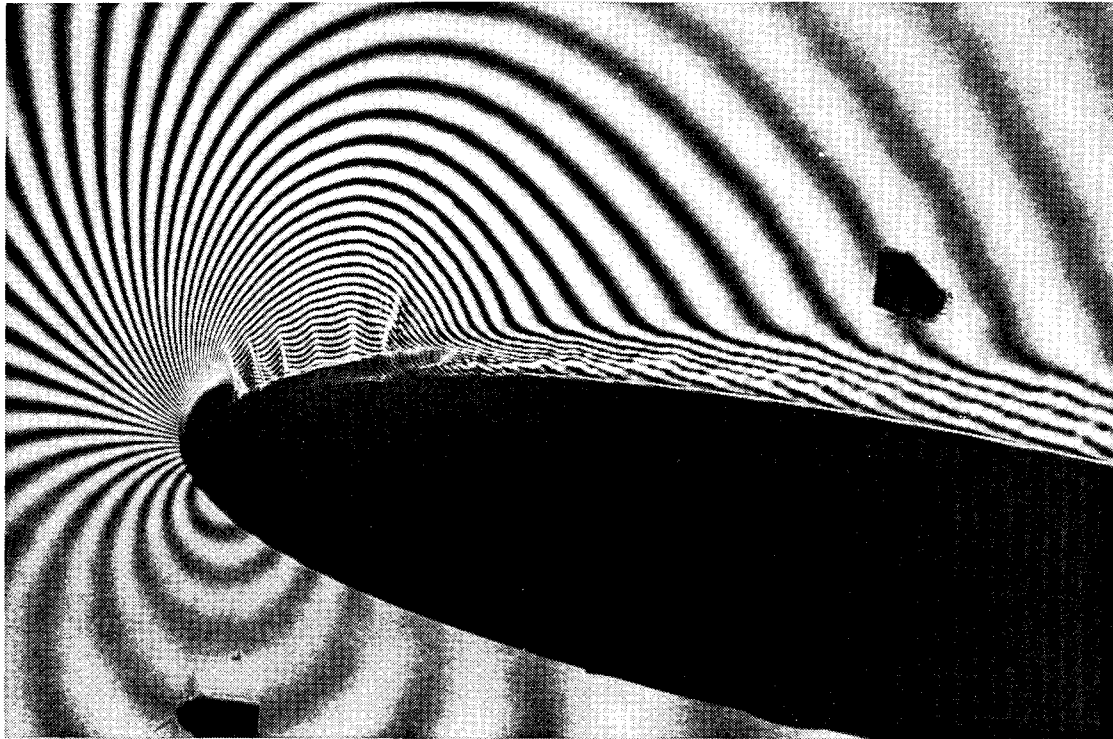


Fig. 10. PDI Image of Multiple Shocks Over Untripped Oscillating Airfoil:  $M = 0.45$ ,  $k = 0.05$ ,  $\alpha = 10^\circ$

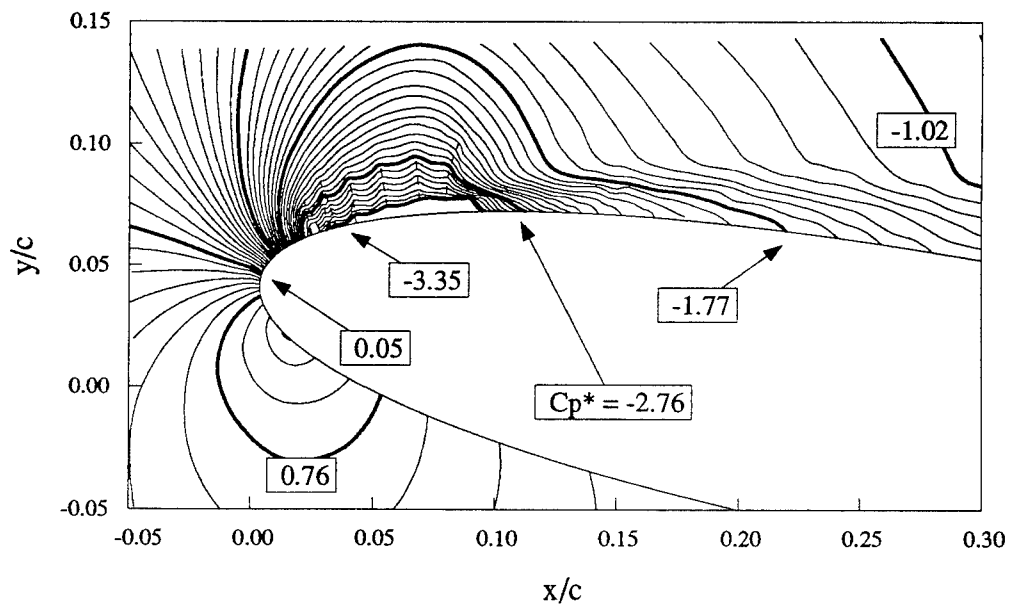


Fig. 11. Global Pressure Field Over Untripped Airfoil from Image in Fig. 10



(a)



(c)



(b)



(d)

Fig. 12. Interferograms of Reattachment Process:  $M = 0.3$ ,  $k = 0.05$ ; (a)  $\alpha = 12.27^\circ$ , (b)  $\alpha = 10.69^\circ$ , (c)  $\alpha = 9.84^\circ$ , (d)  $\alpha = 8.01^\circ$ .

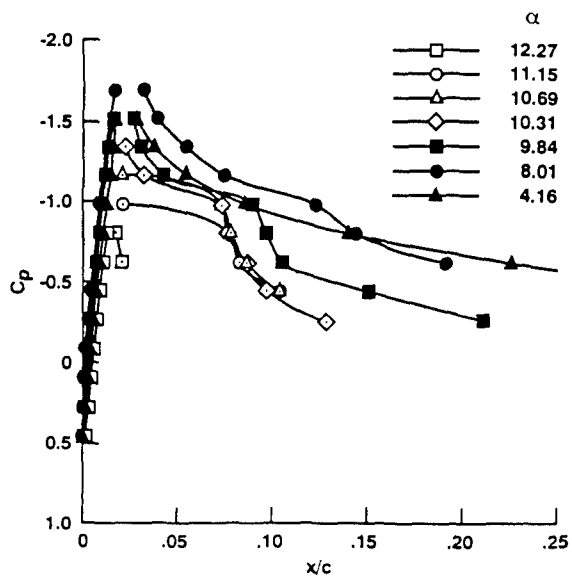


Fig. 13. Pressure Distributions During the Reattachment Process:  $M = 0.3$ ,  $k = 0.05$

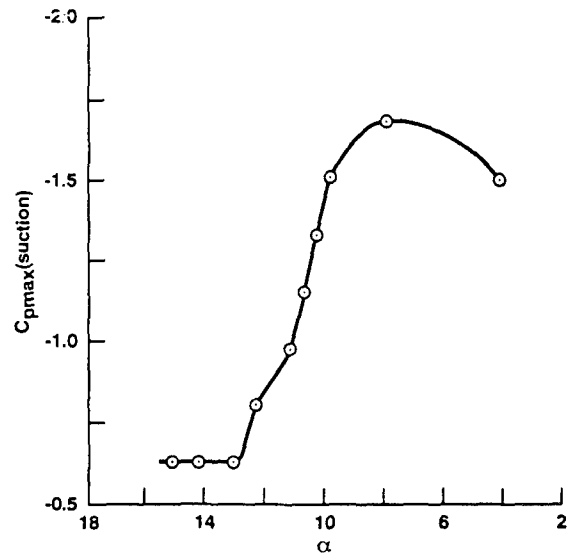


Fig. 14. Variation of Airfoil Suction Peak During the Reattachment Process:  $M = 0.3$ ,  $k = 0.05$

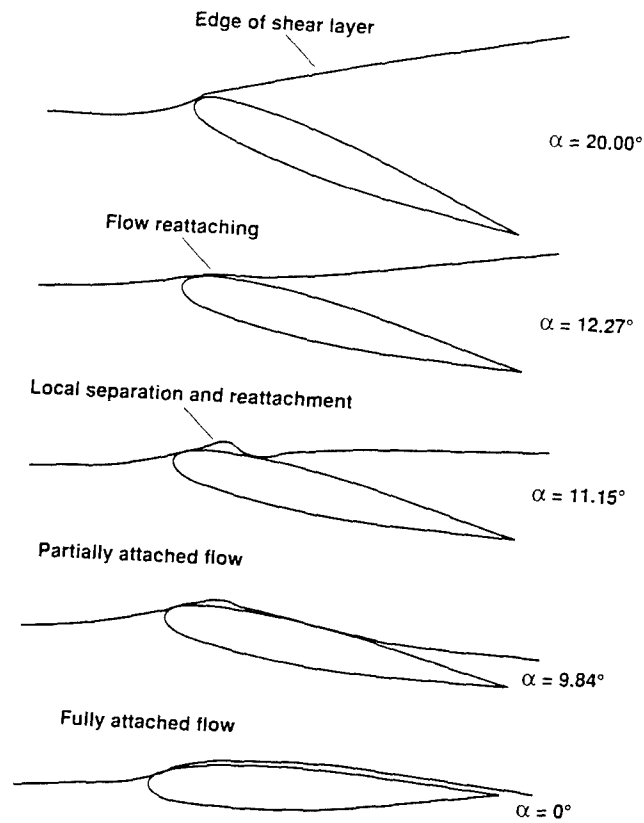


Fig. 15. Schematic of the Reattachment Process

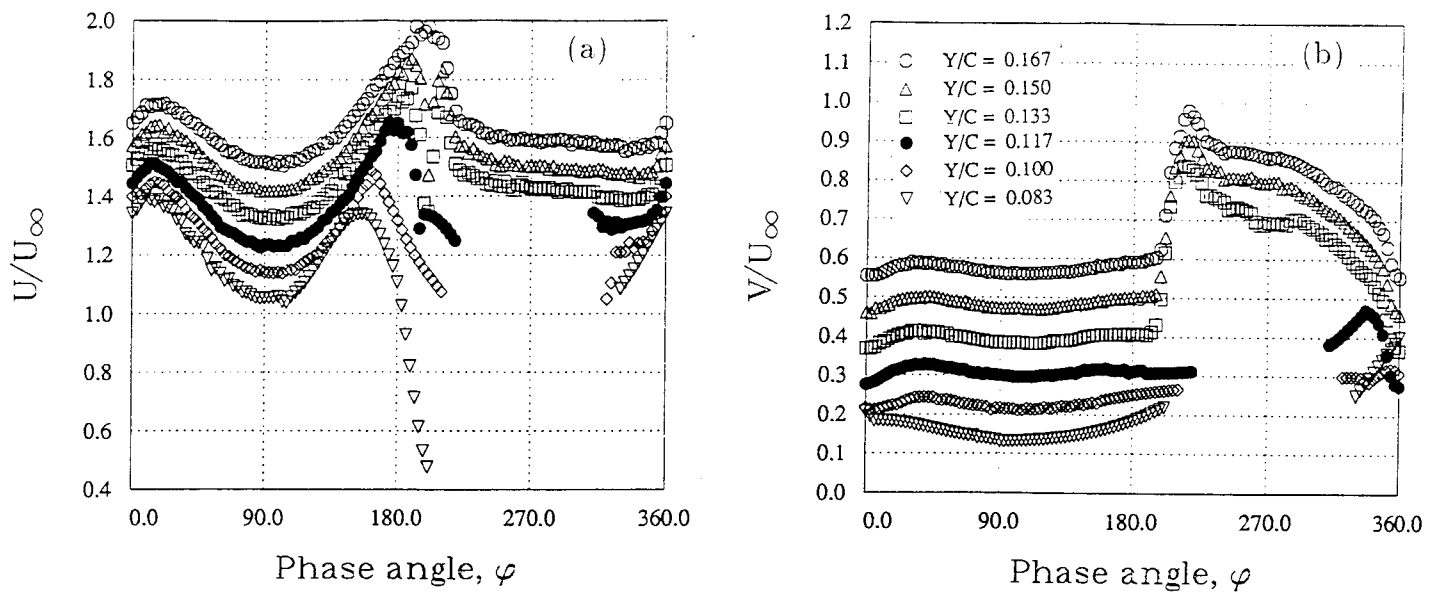


Fig. 16. Phase Distribution of Velocity:  $\alpha = 10^0 - 10^0 \sin \omega t$ ,  $M = 0.3$ ,  $k = 0.05$ : (a) Streamwise Component-  $U$ , (b) Vertical Component- $V$

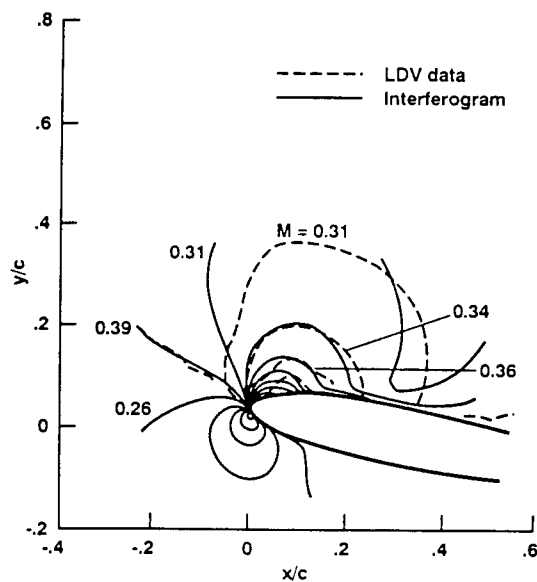


Fig. 17. Comparison of LDV and PDI Data:  $M = 0.3$ ,  $k = 0.05$ ,  $\alpha = 10^0$

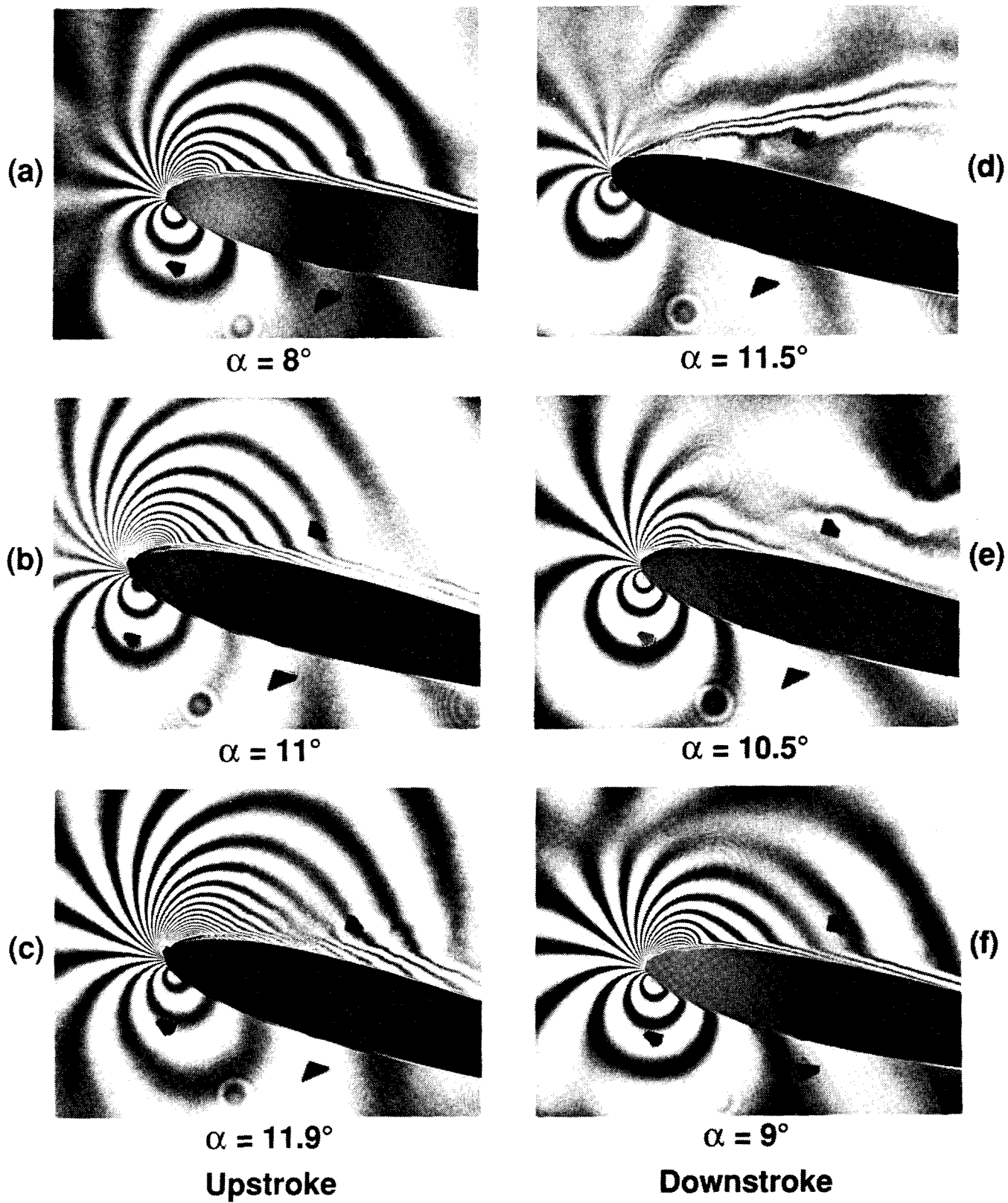


Fig. 18. PDI Sequence of Flow Over Oscillating Airfoil:  $M = 0.3$ ,  $k = 0.05$ ,  $\alpha = 10^\circ - 2^\circ \sin \omega t$

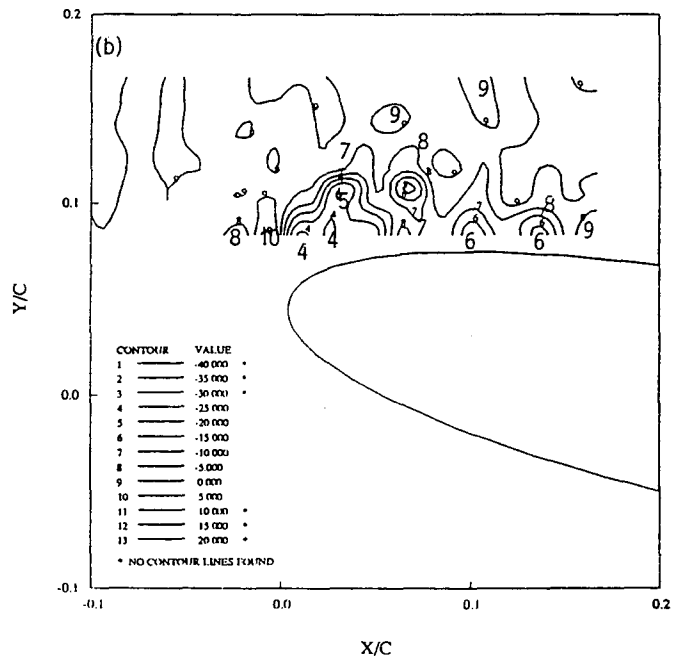
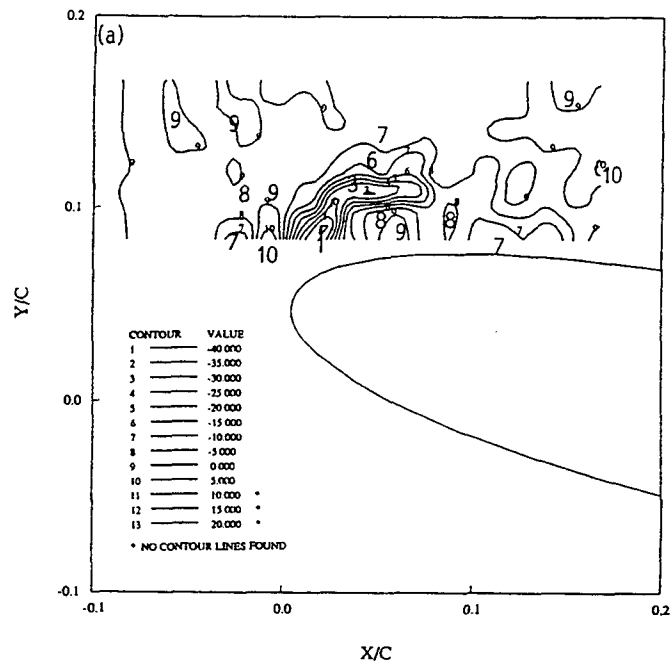
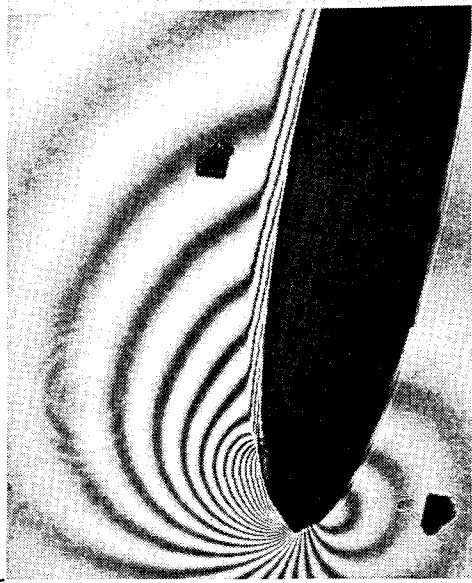
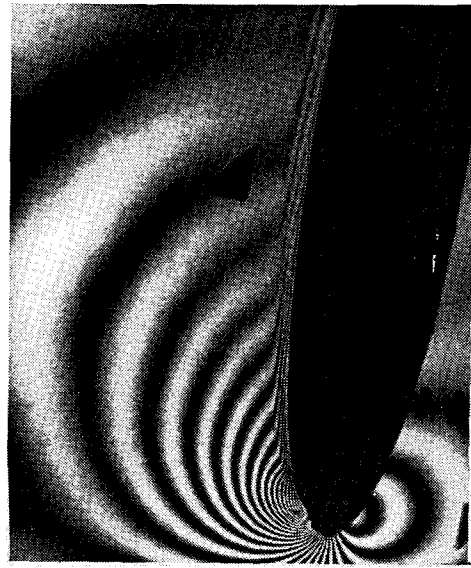


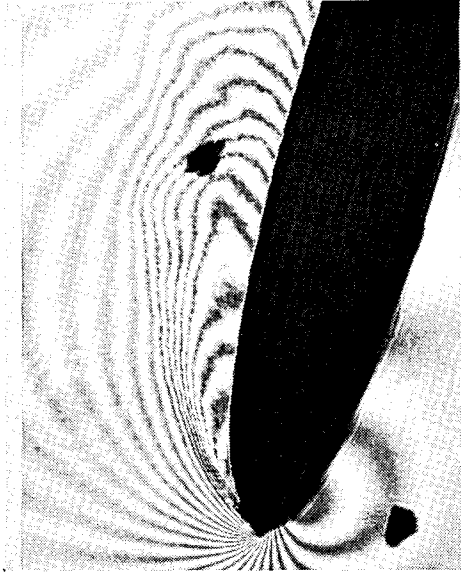
Fig. 19. Contours of Z-component of Vorticity During Airfoil Downstroke:  $M = 0.3$ ,  $k = 0.05$ ,  $\alpha = 10^\circ - 2^\circ \sin \omega t$ ; (a)  $\alpha = 11.53^\circ$ , (b)  $\alpha = 11.0^\circ$



(a)



(b)



(c)



(d)

Fig. 20. PDI Images of Untripped and Tripped Flow Fields:  $M = 0.3$ ,  $k = 0.05$   $\alpha = 10.0^\circ - 10.0^\circ \sin \omega t$ . Top Row: Untripped Airfoil, Bottom Row: Tripped Airfoil, (a,b)  $\alpha = 10.0^\circ$ , (c,d)  $\alpha = 13.99^\circ$

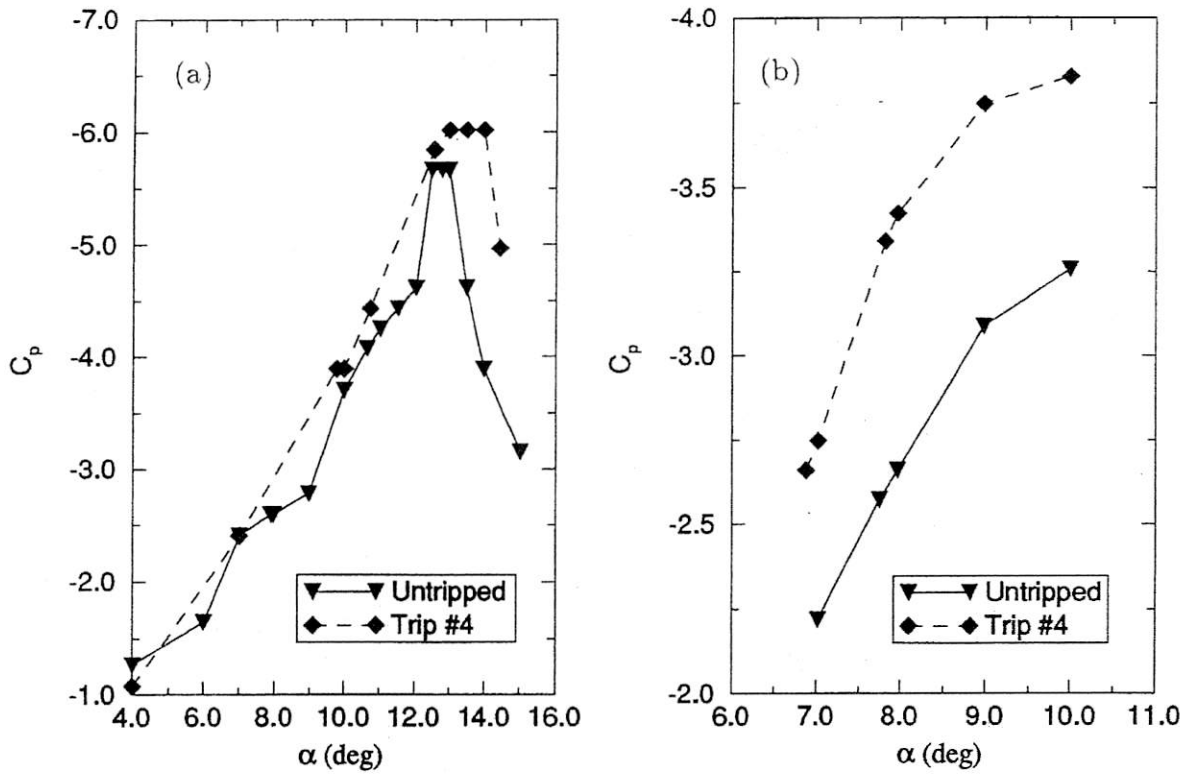


Fig. 21. Effect of Tripping on Airfoil Peak Suction Development:  $\alpha = 10^0 - 10^0 \sin \omega t$ ,  $k = 0.05$ ; (a)  $M = 0.3$ , (b)  $M = 0.45$

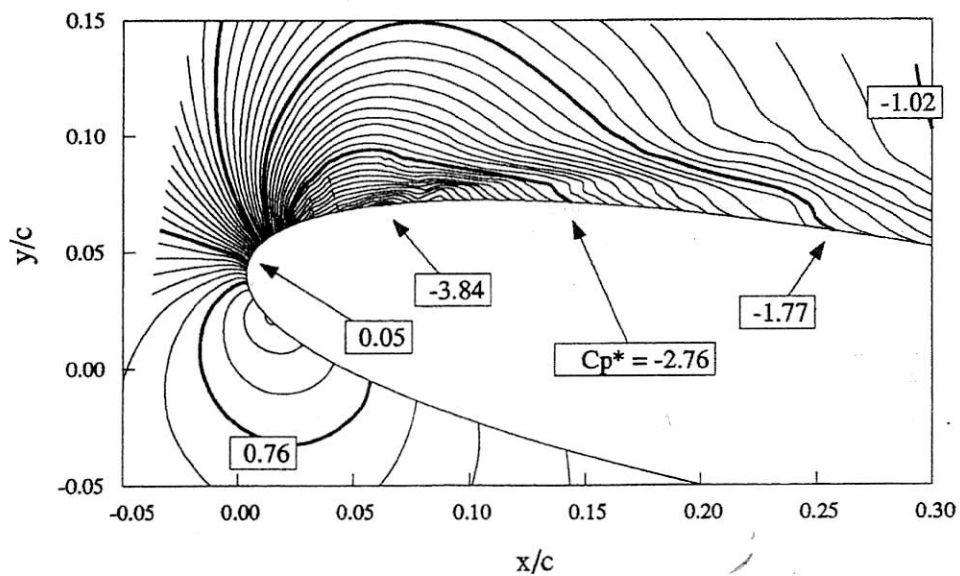


Fig. 22. Global Pressure Field of Shock Flow Over Tripped Airfoil:  $M = 0.45$ ,  $k = 0.05$ .  $\alpha = 10.0^0$

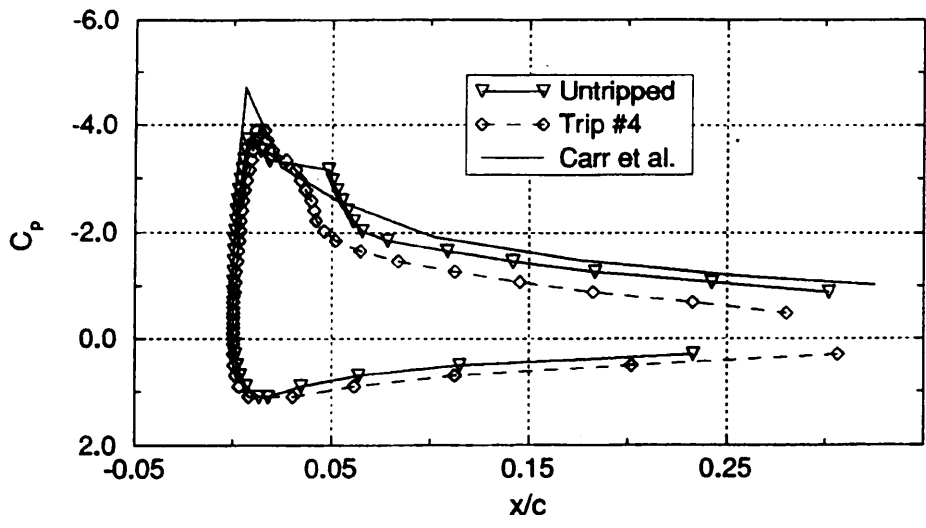


Fig. 23. Comparison of Surface Pressure Distributions Over Oscillating Airfoil in Untripped, Tripped and High Reynolds Number Flows:  $M = 0.3$ ,  $k = 0.05$ ,  $\alpha = 10^\circ$

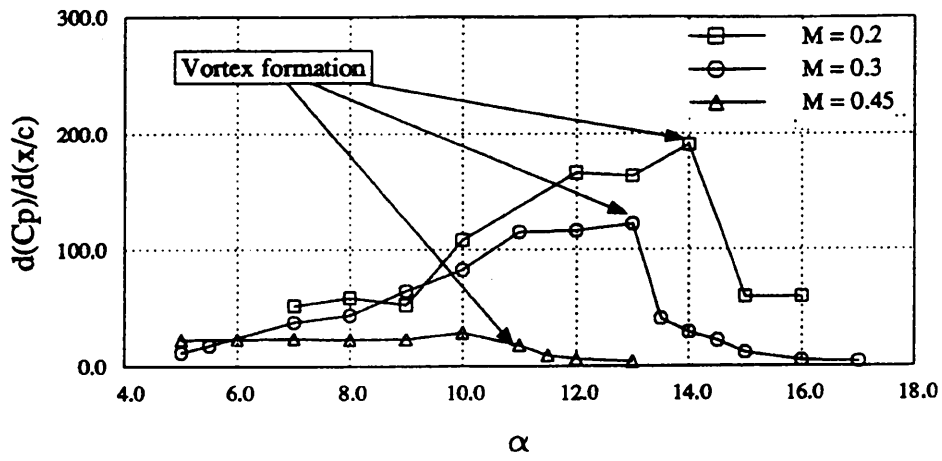


Fig. 24. Mach Number Effect on Leading Edge Adverse Pressure Gradient Development on Transiently Pitching Tripped Airfoil:  $\alpha^+ = 0.03$

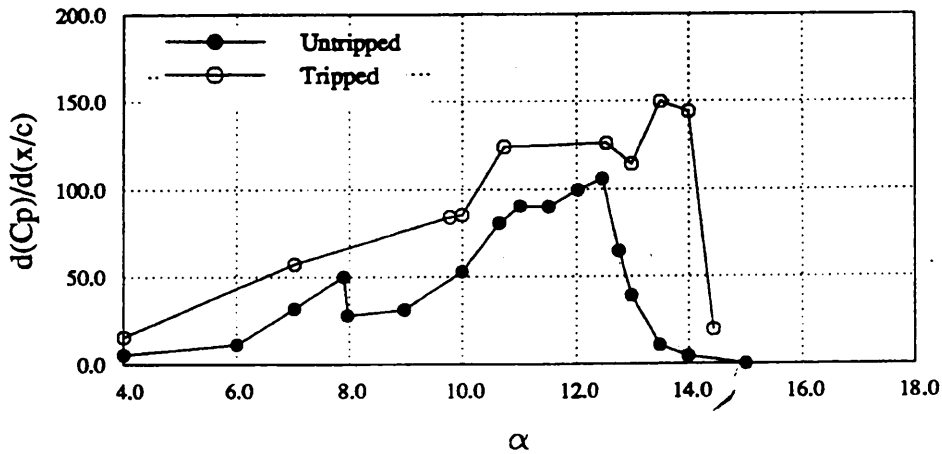


Fig. 25. Leading Edge Adverse Pressure Gradient Development Over Untripped and Tripped Oscillating Airfoil:  $M = 0.3$ ,  $k = 0.05$